EJN fens European Journal of Neuroscience

European Journal of Neuroscience, Vol. 38, pp. 2864–2883, 2013 doi:10.1111/ejn.12287

NEUROSYSTEMS

Synchronisation hubs in the visual cortex may arise from strong rhythmic inhibition during gamma oscillations

Stefanos E. Folias,[1,2] Shan Yu,[3] Abigail Snyder,[2] Danko Nikolić[3,4,5,6] and Jonathan E. Rubin[2,7]
[1]Department of Mathematics and Statistics, University of Alaska Anchorage, Anchorage, AK, USA
[2]Department of Mathematics, University of Pittsburgh, Pittsburgh, PA, USA
[3]Department of Neurophysiology, Max Planck Institute for Brain Research, Frankfurt/Main, Germany
[4]Frankfurt Institute for Advanced Studies, Wolfgang Goethe University, Frankfurt/Main, Germany
[5]Ernst Strüngmann Institute for Neuroscience in Cooperation with Max Planck Society, Frankfurt/Main, Germany
[6]Department of Psychology, University of Zagreb, Zagreb, Croatia
[7]Center for the Neural Basis of Cognition, Pittsburgh, PA, USA

Keywords: cat, computational model, Michigan probes, orientation selectivity, synchronisation

Abstract

Neurons in the visual cortex exhibit heterogeneity in feature selectivity and the tendency to generate action potentials synchronously with other nearby neurons. By examining visual responses from cat area 17 we found that, during gamma oscillations, there was a positive correlation between each unit's sharpness of orientation tuning, strength of oscillations, and propensity towards synchronisation with other units. Using a computational model, we demonstrated that heterogeneity in the strength of rhythmic inhibitory inputs can account for the correlations between these three properties. Neurons subject to strong inhibition tend to oscillate strongly in response to both optimal and suboptimal stimuli and synchronise promiscuously with other neurons, even if they have different orientation preferences. Moreover, these strongly inhibited neurons can exhibit sharp orientation selectivity provided that the inhibition they receive is broadly tuned relative to their excitatory inputs. These results predict that the strength and orientation tuning of synaptic inhibition are heterogeneous across area 17 neurons, which could have important implications for these neurons' sensory processing capabilities. Furthermore, although our experimental recordings were conducted in the visual cortex, our model and simulation results can apply more generally to any brain region with analogous neuron types in which heterogeneity in the strength of rhythmic inhibition can arise during gamma oscillations.

Introduction

In the primary visual cortex, the firing of excitatory neurons is modulated by stimulus features, such as orientation. Neurons sharing similar preferred orientations (i.e. the orientation that elicits the strongest response in a given neuron) are distributed spatially to form an orientation map (Gilbert & Wiesel, 1983; Blasdel, 1992; Bosking *et al.*, 1997;). Even within spatially contiguous domains where excitatory neurons have similar orientation preferences, however, other firing properties, such as orientation tuning curve width (Bonds, 1989; Sato *et al.*, 1996; Ringach *et al.*, 2002; Li *et al.*, 2008; Nauhaus *et al.*, 2008; Nowak *et al.*, 2008; Yu *et al.*, 2008; Nikolić, 2009) and oscillation strength (Nikolić, 2009), can be highly variable across cells.

In previous work (Yu *et al.*, 2008) that examined synchronisation among the excitatory neurons of cat area 17, the results of a connectivity analysis on unit recordings revealed that a subset of neurons, termed hubs, tended to synchronise particularly strongly and promiscuously with other area 17 neurons. Indeed, even neurons with differing orientation preferences tended to synchronise if they were hubs. Notably, neurons exhibiting sharp orientation tuning curves showed a strong likelihood of being hubs. To avoid confusion with other uses of 'hubs' in the literature, we henceforth refer to these promiscuous synchronisers as synchronisation hubs (SHs) and other neurons as not synchronisation hubs (nSHs).

We reasoned that the existence and characteristics of SHs could provide clues about the nature of the connectivity properties within area 17. Therefore, we set out to explain the mechanisms underlying the emergence of SHs during gamma oscillations that are commonly observed in cat area 17 (Gray & Singer, 1989; Gray *et al.*, 1989; Samonds & Bonds, 2005). To achieve this goal, we recorded neuronal activities extracellularly from cat area 17 using microelectrode arrays and systematically analysed visual responses in terms of orientation

Correspondence: Stefanos E. Folias, [1]Department of Mathematics and Statistics, as above.
E-mail: sfolias@uaa.alaska.edu

Received 21 January 2013, revised 14 May 2013, accepted 29 May 2013

selectivity, oscillation within the beta/gamma range and synchronisation among spatially distributed units. Furthermore, we developed and simulated a computational model to test a potential mechanism that could produce SHs with the properties that we observed experimentally. Our simulations support the idea that strong, broadly tuned rhythmic inhibition to SHs underlies the features exhibited in our recordings. We propose that this inhibition causes SHs to exhibit enhanced oscillations and synchrony and to maintain oscillations and synchronisation with other neurons, despite sharp drops in firing rates when stimulus optimality is decreased.

Materials and methods

Experiments

Preparation

In three cats, anesthesia was induced with ketamine and, following a tracheotomy, was maintained with a mixture of 70% N_2O and 30% O_2 and with halothane (0.6%). To prevent eye movements, the cat was paralyzed with intravenous pancuronium bromide [Pancuronium, Organon, 0.15 mg/(kg·h)]. All experiments were conducted in accordance with the Society for Neuroscience, German law, and the European Communities Council Directive of 24 November 1986 (86/609/EEC) regarding the care and use of animals for experimental procedures, approved by the local government's ethical committee (Regierungspräsidium Darmstadt), and overseen by a veterinarian.

Recordings

Multi-unit activity (MUA) was recorded from area 17 in cat using a silicon-based 16-channel probe (organised in a 4×4 spatial matrix) supplied by the Center for Neural Communication Technology at the University of Michigan. Each probe consisted of four 3-mm long shanks that were separated by 0.2 mm and each contained four electrode contacts (surface area of the contact, 1250 μm^2; impedance, 0.30–0.5 MΩ at 1000 Hz; intercontact distance, 0.2 mm). The probes were inserted such that the last row of contacts was submerged about 0.2 mm into the cortex. Therefore, the probes recorded primarily the activity of superficial layers. Signals were amplified 1000 times, filtered between 500 Hz and 3.5 kHz, and digitised with a 32-kHz sampling frequency. Each probe was inserted into the cortex approximately perpendicular to the surface, which allowed recording simultaneously from neurons at different depths and with different orientation preferences. The borders of receptive fields for each unit were mapped manually, i.e. bar stimuli were moved by hand and the borders were determined by locations in the visual field at which a noticeable change in the firing rate could be detected by both listening to the activity of that unit fed into a speaker and monitoring the same signal on an oscilloscope. Within each probe, all of the receptive fields were overlapping and were therefore all stimulated simultaneously by a single stimulus.

Stimulation

Stimuli were presented monocularly on a 21-inch computer monitor (Hitachi CM813ET) with a 100-Hz refresh rate. To obtain binocular fusion, the optical axes of the two eyes were first determined by mapping the borders of binocular receptive fields from responses to moving single bars, and then the optical axes were aligned on the computer screen with adjustable prisms placed in front of one eye. The software for visual stimulation was a commercially available stimulation tool, ActiveSTIM (\www.ActiveSTIM.com). All receptive fields were determined by manually mapping with high-contrast white bars on a black background. Because of the spatial proximity of the electrode contacts, the receptive fields recorded from one probe always overlapped, producing clusters that spanned up to 10° of visual angle. The stimuli were always positioned such that their centers matched the center of the receptive field cluster. All visual stimuli consisted of high contrast ($C = 0.94$) sinusoidal gratings of 12° visual angle in diameter, chosen to cover the cluster of the receptive field. Gratings drifted orthogonally relative to their orientations in 12 different directions (0, 30, 60, …, 330°). The spatial frequency, size, and moving speed of the gratings were 2.4°/cycle, 12°, and 2°/s, respectively. The choice of these values was driven by the typical response properties of neurons in cat area 17, thus maximising the average degree of activation across the entire population of recorded neurons. Judging by poststimulus time histograms and tuning curves, the stimuli clearly produced responses in each unit in at least one drifting direction. A total of 20 trials were conducted and, during each trial, all 12 stimulus directions were presented for 3–5 s each with an interstimulus interval of about 2 s. The order of condition presentations was block-randomised. Single-unit activity (SUA) was extracted by applying an offline spike-sorting procedure based on principal component analysis of spike wave forms. Tuning curves for direction selectivity, rastergrams, crosscorrelograms, and autocorrelograms were computed from both SUA and MUA (see Data analysis).

Data analysis

Orientation tuning curves

Tuning curves for recorded MUA and SUA were generated based on the firing rate responses to sinusoidal gratings drifting in 12 different directions by calculating the average firing rate over the sustained response for each direction (from 1.0 s after stimulus onset to immediately before the stimulus offset) and averaging over all trials. Firing rates were measured in units of spikes/s to distinguish them from the frequencies of oscillatory signals or the frequencies at which spike trains were modulated, which were measured in units of Hz.

Orientation selectivity

Orientation selectivity was quantified for each recorded unit with a previously established method (Leventhal *et al.*, 1995). The responses to various ($k = 1, 2, \ldots 12$) stimulus orientations θ_k (°) were represented as vectors, with the response amplitude r_k (spikes/s) as the magnitude and twice the stimulus orientation as the angle. Such response vectors for all orientations were first added and then divided by the sum of their magnitudes to obtain the vector R, i.e.

$$R = \frac{\sum_k r_k e^{i2\theta_k}}{\sum_k r_k}$$

The magnitude $|R|$ of the resulting vector was named the orientation bias and served as a measure of the orientation selectivity. Orientation bias takes values between 0 and 1 with an orientation bias value close to 1 indicating strong orientation selectivity and 0 indicating null selectivity. Note that the orientation bias is related to the circular variance (Ringach *et al.*, 2002) by the relation: (circular variance) = 1 – (orientation bias).

Oscillation strength

To quantify the oscillation strength of the recorded neuronal responses, we computed the oscillation score, as described previously (Muresan *et al.*, 2008). In brief, this measure is based on analysing the power spectrum of autocorrelation histograms (ACHs) computed with 1-ms resolution (see below). The oscillation score is defined as the ratio between the peak magnitude in the frequency band of interest and the mean magnitude of the spectrum. In our case, the band of interest covered the upper beta/lower gamma band (25–35 Hz); for brevity, we refer to this as a gamma band in the remainder of the article. The oscillation score has been demonstrated to be a good measure of oscillation strength for neuronal activity (Muresan *et al.*, 2008) based on its simplicity and robustness under various conditions (e.g. low spike count). The MATLAB code for implementing the oscillation score calculation can be found in Muresan *et al.* (2008). To quantify the oscillation strength of simulated neuronal responses, the ratio between the height of the first satellite peak in the fitting function and the mean of the ACH was used to quantify the strength of the oscillatory response; this method was used for simulation results because the strength of the oscillations in the output of the neurons was controlled and predicted by the strength of the rhythmic inputs. In general, both of the above methods for computing the oscillation strength gave highly consistent results.

Synchrony strength

The spike trains of individual units were first converted into binary variables $X = \{x_1, x_2, \cdots\}$ and $Y = \{y_1, y_2, \cdots\}$ (where each component is 1 if a spike occurred and 0 if there was no spike, with 3-ms binning). We next computed the Pearson correlation coefficient

$$r = \sum_i \frac{\langle (x_i - \bar{x})(y_i - \bar{y}) \rangle}{\sigma_x \sigma_y} = \sum_i \frac{\langle x_i y_i \rangle - \bar{x}\,\bar{y}}{\sigma_x \sigma_y}$$

where $\langle \cdot \rangle$ is the expectation, $\bar{x}$ and $\bar{y}$ are means, and σ_x and σ_y are SDs of X and Y, respectively. For binary time series, $\sigma_x = \sqrt{\bar{x}(1-\bar{x})}$. The Pearson correlation coefficient scales the number of coincidences above baseline by the product of the SDs for two time series. To exclude the potential influence of rate covariation locked to stimulus onset, a corrected measure of the correlation was obtained by subtracting the Pearson correlation coefficient of trial-shuffled activities from the original correlation coefficient. The synchrony strength for a given unit was then defined as the mean of the corrected correlations between that unit and all other units recorded by the same probe. The results were based on visual responses in all conditions (cf. Fig. 3) or the optimal condition only (cf. Fig. S1). In all cases, only the sustained responses (from 1.0 s after stimulus onset to immediately before the stimulus offset) were included for analysis.

To exclude contributions of slow rate covariations that were not locked to the stimulus onset, the synchrony strength was also quantified by scaled correlation, a recently introduced method (Nikolić *et al.*, 2012) that provides a measure of correlation for specifically chosen temporal scales. In this case, scaled correlation was computed for a scale suitable for correlation in the beta/gamma frequency range (scale $s = 35$ ms for Cat 1 and 25 ms for Cat 2, which correspond to the peak oscillation frequencies estimated by computing autocorrelations) for all neuronal pairs, with 1-ms binning. Pairwise correlation was then quantified by the summation of the three center entries (i.e. time lags of −1, 0 and 1 ms). In this case, the synchrony strength for a given unit was defined as the mean of the scaled correlations between that unit and all other units recorded by the same probe.

Autocorrelograms/crosscorrelograms

The ACHs and crosscorrelation histograms (CCHs) are graphical representations of the set of all spike time differences between two spike trains and are useful for highlighting synchrony and oscillatory modulation of the firing output of neurons. The difference between the two is that CCHs are computed from spike trains in two different units, whereas ACHs are computed only from one spike train against itself. ACHs/CCHs were computed by (i) calculating the pairwise difference $t_n^1 - t_m^2$ between each of the spike times in two spike trains (i.e. for all m and n, where $t_1^1, t_2^1, t_3^1, \cdots, t_N^1$ are the spike times in one spike train and $t_1^2, t_2^2, t_3^2, \cdots, t_M^2$ are the spike times in the other spike train), and (ii) plotting a normalised histogram of these time differences (lags), in 1-ms bins, over the interval [−80, 80 ms].

As with the orientation tuning curve, all figures for the experimental recordings were generated using the sustained response. For simulations, it was not necessary to cut out an initial data segment because our model was designed to describe sustained responses only and hence did not exhibit a pronounced initial transient response to the stimulus. In all figures, the CCHs and ACHs were normalised, with the vertical axis representing the ratio (count in each 1-ms bin) : (baseline count in each 1-ms bin). For experimental recordings, the baseline count was estimated by taking the average count per bin in the ACH/CCH over the lag intervals [−300, −150 ms] and [150, 300 ms], which were intervals at which the oscillatory patterning first became discernibly attenuated such that the ACH/CCH was relatively flat. In simulations, the baseline count was computed (i) as described in the experimental case, or (ii) by generating an ACH/CCH using one or two neurons driven with excitatory inputs generated by a homogeneous Poisson process (i.e. without the oscillatory component) to fire at the same rate as the neurons of interest.

Coincidence measure

We defined the coincidence measure between two units to be represented by the size of the CCH center peak (around 0 lag) relative to the baseline count within a corresponding time window using the following pairwise measure: (size of the center peak)/(baseline count) – 1. Equivalently, this measure is defined as (the number of coincidences above baseline count)/(baseline count). When multiplied by 100, the coincidence measure represents the increase in the number of coincidences relative to the baseline count (given as a percentage). We calculated this measure for three different time windows ($N = 1$, 3, 5 ms) about 0 lag and all gave qualitatively similar results. In Figs 2, 4, 8 and 9 in this article, the coincidence measure was computed using only a time window spanning 3 ms about 0 lag. Note that, in contrast to the synchrony strength, the coincidence measure was based on spike times rather than binary time series computed from spike trains. However, for comparison with the synchrony strength, the expression for the coincidence measure computed for binary time series would be given by

$$\sum_i \frac{\langle x_i y_i \rangle - \bar{x}\,\bar{y}}{\bar{x}\,\bar{y}}$$

Simulations

Neuron model

Each neuron was represented by a single-compartment model governed by either conductance-based or integrate-and-fire dynamics. In the integrate-and-fire model, the membrane potential V obeyed the differential equation (Dayan & Abbott, 2005)

$$C_m \frac{\mathrm{d}V}{\mathrm{d}t} = -g_L(V - E_L) + I^{\mathrm{syn}}(t)$$

with a spike occurring when V is increased through the threshold $V_{\mathrm{th}} = -55$ mV, at which point V was reset to $V_{\mathrm{reset}} = -75$ mV. The term $I^{\mathrm{syn}}(t)$ represents the collection of all synaptic current inputs to the neuron, and $C_m = 1$ pF, $g_L = 0.02$ mS/cm^2 and $E_L = -70$ mV. Numerical integration was performed using either an Euler or an improved Euler method, with the threshold crossing computed more precisely using linear interpolation between the two consecutive time points straddling the threshold. Conductance-based models yielded similar results (not shown); however, as the integrate-and-fire model is substantially less numerically intensive to simulate, it was selected as the practical choice for extensively exploring various features of the model.

We considered collections of either four or six model neurons with identical intrinsic dynamics. These were assumed to represent excitatory neurons in cat area 17. Direct synaptic connections between these neurons were not included in the model. In the absence of any input, each model neuron remained at rest (the leak reversal potential E_L for the integrate-and-fire model) and, otherwise, the firing output of each neuron was predominantly shaped by the synaptic input it received. To simulate excitatory cell firing during gamma oscillations, we prescribed three types of synaptic currents to each neuron, each generated stochastically according to a Poisson process: (i) $I_i^{\mathrm{osc}}(t)$, rhythmic inhibitory ($GABA_A$-mediated) input that oscillates in the gamma frequency range, (ii) $I_e^{\mathrm{hom}}(t)$, excitatory (AMPA-mediated) synaptic input generated by a homogeneous Poisson process, and (iii) $I_e^{\mathrm{non}}(t)$, gamma-modulated excitatory (AMPA-mediated) synaptic input generated by a non-homogeneous Poisson process. We describe in detail below how each component was computed, with the total synaptic current $I^{\mathrm{syn}}(t)$ calculated as

$$I^{\mathrm{syn}}(t) = I_i^{\mathrm{osc}}(t) + I_e^{\mathrm{hom}}(t) + I_e^{\mathrm{non}}(t)$$

Simulations that were performed over intervals of 10–60 s of time and over hundreds of independent trials generated sufficient single neuron data to produce smooth auto/crosscorrelograms (see Data analysis). (For code see ModelDB accession no. 150241).

Rhythmic inhibitory input and the gamma cycle

To introduce an inhibitory input that exhibited a gamma oscillation, on each trial j, we defined a sequence of gamma cycle start times $T_{j,n}$ calculated iteratively as $T_{j,n+1} = T_{j,n} + \delta T_{j,n}$ where $T_{j,n}$ denotes the start of the nth cycle on trial j. The quantity $\delta T_{j,n}$ denotes the length of the nth cycle on trial j, and it was assumed to vary stochastically across cycles (described separately in detail below). The profile of the cumulative or summated inhibitory synaptic conductance $s_i(t)$ during the nth cycle ($T_{j,n} < t < T_{j,n+1}$) on trial j was prescribed by an alpha function

$$s_i(t) = \gamma_n[0.07(t - T_{j,n})^2 \exp(-(t - T_{j,n})/4)]$$

The factor $\gamma_n = (T_{j,n+1} - T_{j,n})/T_j$, where ω_j and $T_j = \omega_j^{-1}$ $(1000\,ms/s)$ denote the average frequency and average cycle length of the oscillation on trial j, respectively, modulated the conductance amplitude on each cycle, slightly increasing the amplitude for cycle lengths longer than average, and slightly decreasing the amplitude for cycles shorter than average. As the GABAergic basket cells that are believed to mediate gamma oscillations *in vivo* (Tamás *et al.*, 2000; Freund, 2003; Gloveli *et al.*, 2005; Middleton *et al.*, 2008; Whittington *et al.*, 2010) each contact a large number of excitatory neurons and often form multiple boutons on the soma or perisomatic region of each neuron, they exert strong and rapid synaptic control over the firing output of excitatory neurons (Martin *et al.*, 1983; Somogyi *et al.*, 1983; Kisvárday & Eysel, 1993). The alpha function profile was tuned to be representative of the superposition of a barrage of synaptic inputs from a collection of these inhibitory neurons firing approximately synchronously, with firing times distributed over the early part of each gamma cycle. This timing profile is consistent with the assumption that the inhibitory synaptic inputs based on $GABA_A$-mediated currents have similar decay time constants, commensurate with the mean cycle length within the oscillation.

The total inhibitory synaptic current was calculated as

$$I_i^{\mathrm{osc}}(t) = -g_i s_i(t)(V(t) - E_i^{\mathrm{syn}}),$$

using the inhibitory reversal potential $E_i^{\mathrm{syn}} = -75$ mV and a maximal effective conductance or effective conductance strength g_i that was varied across simulations (values are listed in Table 1). As time progressed within each cycle, the summated conductance profile $s_i(t)$ decayed, reaching less than 5% of its maximum during the final 5–15 ms of the cycle. In simulations of four or six model neurons receiving perfectly in-phase rhythmic inhibition, the synaptic inhibitory currents $I_i^{\mathrm{osc}}(t)$ to all cells had the same profile $s_i(t)$, whereas the effective conductance strength g_i was allowed to vary from neuron to neuron. Importantly, this input generation method allowed the cycle length of the gamma oscillation to vary stochastically while maintaining oscillations in the rhythmic inhibitory input that are perfectly in phase across neurons.

Excitatory input I_e^{hom} (t) (homogeneous Poisson generated)

One component of the excitatory synaptic input current was assumed to be generated from a homogeneous Poisson process. More precisely, excitatory postsynaptic currents were activated at spike times selected from an exponential distribution with rate r_{hom}. The rate r_{hom} was allowed to vary from neuron to neuron and was viewed as being representative of the collective inputs from many different excitatory neurons firing independently. A corresponding excitatory conductance was produced by convolving the train of spike times (i.e. a sum of δ-functions ordered in time according to the index spk = 1 … N) with an alpha function that was representative of an AMPA-receptor mediated excitatory synapse. This convolution yielded a conductance profile $S_{e,\mathrm{spk}}(t)$, arising from a spike occurring at $t = \tau_{\mathrm{spk}}$, given by

$$s_{e,\mathrm{spk}}(t) = \begin{cases} (t - \tau_{\mathrm{spk}})\exp(-(t - \tau_{\mathrm{spk}})/2), & t > \tau_{\mathrm{spk}}, \\ 0, & t \le \tau_{\mathrm{spk}} \end{cases} \quad (1)$$

The excitatory postsynaptic current $I_{e,\mathrm{spk}}^{\mathrm{hom}}(t)$ resulting from the spike at $t = \tau_{\mathrm{spk}}$ was computed as

$$I_{e,\mathrm{spk}}^{\mathrm{hom}}(t) = -g_e s_{e,\mathrm{spk}}(t)(V(t) - E_e^{\mathrm{syn}}), \quad (2)$$

where $V(t)$ was the membrane potential of the postsynaptic cell. The accumulated excitatory postsynaptic current arising from the spike train was given by

TABLE 1. Model parameters for Figs 8–11

	Label	g_i	r_{hom}	r_{non}
Parameters for Fig. 8*				
A–D	1	0.01	0.14	0.035
	2	0.025	0.14	0.070
	3	0.05	0.14	0.133
	4	0.1	0.14	0.210
E	nSH	0.04	0.214	–
	SH	0.08	0.270	–
F	nSH	0.04	0.075	0.098
	SH	0.08	0.15	0.173
Parameters for Fig. 9†				
A	1 - nSH	0.045	0.148	0.096
	2 - SH	0.09	0.148	0.185
	3 - SH	0.09	0.148	0.185
	4 - nSH	0.045	0.148	0.096
B	1 - nSH	0.045	0.148	0.096
	2 - SH	0.09	0.148	0.185
	3 - SH	0.045	0.096	0.096
	4 - nSH	0.02	0.096	0.051
Parameters for Fig. 10‡	All	0.08	0.148	0.163
Parameters for Fig. 11§				
Solid gray	0	0.04	0.148	0.089
	1	0.03	0.130	0.067
	2	0.02	0.109	0.044
	3	0.01	0.089	0.022
Solid black	0	0.08	0.148	0.178
	1	0.06	0.130	0.133
	2	0.04	0.109	0.089
	3	0.02	0.089	0.044
Dashed black	0	0.08	0.148	0.178
	1	0.07	0.130	0.133
	2	0.06	0.109	0.089
	3	0.05	0.089	0.044

*Common parameters for Fig. 8: ω = 30 Hz, $\Delta\omega_{\text{trial}}$ = 3 Hz, $\Delta\omega_{\text{cycle}}$ = 4. †Common parameters for Fig. 9: ω = 30 Hz, $\Delta\omega_{\text{trial}}$ = 3 Hz, $\Delta\omega_{\text{cycle}}$ = 6. ‡Common parameters for Fig. 10: ω = 30 Hz, $\Delta\omega_{\text{trial}}$ = 4 Hz, $\Delta\omega_{\text{cycle}}$ = 4. Columns 1 and 2 correspond to jitters $\delta v_{j,n}^1$ and $\delta v_{j,n}^2$ where (A) Δv_{cycle} = 0.25 1/ms, (B) Δv_{cycle} = 0.5 1/ms, (C) Δv_{cycle} = 1.0 1/ms. §Common parameters for Fig. 11: ω = 33 Hz, $\Delta\omega_{\text{trial}}$ = 3 Hz, $\Delta\omega_{\text{cycle}}$ = 6.

$$I_e^{\text{hom}}(t) = \sum\nolimits_{\text{spk}=1}^{N} I_{e,\text{spk}}^{\text{hom}}(t) \tag{3}$$

All excitatory synaptic inputs to all neurons were computed with conductance strength g_e = 0.01 mS/cm^2 and reversal potential E_e^{syn} = 0 mV.

Excitatory input $I_e^{\text{non}}(t)$ (gamma modulated)

We assumed that some of the excitatory synaptic inputs to each excitatory neuron would be generated by other excitatory neurons subject to the same gamma-modulated inhibition to which it was exposed. Therefore, in our simulations, each neuron received a second excitatory synaptic current component. $I_e^{\text{non}}(t)$ that was generated from a non-homogeneous Poisson process, modulated in the gamma frequency range. To create the non-homogeneous process, we initially generated spikes from a homogeneous Poisson process with rate r_{non}; spikes were subsequently deleted based on their timing relative to the ongoing inhibitory gamma oscillation, under the assumption that spikes were less (more) likely to occur in the early (late) phase of the gamma cycle, defined as the phase where inhibition was strongest (weakest). Specifically, during the nth gamma cycle $[T_{j,n}, T_{j,n+1}]$, a spike at time t (in ms) was pruned if a number picked from a uniform distribution on [0,1] was below the curve given by

$$H(t) = 0.65 + 0.35[\cos(0.55 + 2\pi(t - T_{j,n})/(T_{j,n+1} - T_{j,n}))]$$

For each spike time $t = \tau_{\text{spk}}$, the resulting excitatory postsynaptic current $I_{e,\text{spk}}^{\text{non}}(t)$ was generated analogously using Eqns (1) and (2), as described above. The total gamma-modulated excitatory component $I_e^{\text{non}}(t)$ was computed similarly to Eqn (3).

Setting the firing rate of the model neuron

The cells were assumed to fire sparsely, skipping most of the cycles of the gamma oscillation (Nikolić, 2009). The average firing rate was controlled by three parameters that we varied across conditions: (i) the strength of the rhythmic inhibition g_i, (ii) the Poisson rate r_{hom} for the homogeneous Poisson process associated with excitatory input, and (iii) the max rate r_{non} for the non-homogeneous Poisson process associated with gamma-modulated excitatory input. When a certain firing rate was desired, we first set the level of g_i and next tuned the parameters r_{hom} and r_{non} to produce the desired output firing rate. To be consistent with our experimental recordings, the average firing rate of any neuron that was considered to be optimally stimulated was set to 10 spikes/s. As the maximal firing rates of both sharply-tuned and broadly-tuned neurons are roughly the same, we assumed that stronger inhibition at preferred orientations would be accompanied by increased local cortical excitation. This assumption is consistent with experimental results (Anderson *et al.*, 2000; Mariño *et al.*, 2005; Atallah & Scanziani, 2009; Isaacson & Scanziani, 2011) showing that the excitatory and inhibitory postsynaptic currents in cat area 17 tend to covary in a way that maintains a balance of inputs.

Stochastic fluctuations in gamma cycle length

We ran repeated simulations of 10–60 s each under each set of conditions considered, referring to each simulation as a trial. Within each trial, many gamma oscillation cycles occurred. Stochastic fluctuations were introduced into the cycle structure of the gamma oscillations in two ways. (i) Within each trial, the cycle length fluctuated stochastically around an average cycle length that was set by a trial-average gamma frequency denoted by ω_j for trial j. The time $T_{j,n+1}$ corresponding to the beginning of the (n + 1)th gamma cycle on trial j was correspondingly computed as $T_{j,n+1} = T_{j,n} + \delta T_{j,n}$ where

$$\delta T_{j,n} = \frac{1000\,ms/s}{\omega_j + \delta\omega_{j,n}}$$

and $\delta\omega_{j,n}$ denotes the cycle-to-cycle jitter on cycle n within trial j, selected from a zero mean normal distribution with a SD $\Delta\omega_{\text{cycle}}$. If a realisation of $\delta\omega_{j,n}$ exceeded $\Delta\omega_{\text{cycle}}$, it was discarded and resampled. (ii) The average gamma frequency ω_j itself was varied across trials, with each ω_j selected from a uniform distribution over $[\omega-\Delta\omega_{\text{trial}}, \omega+\Delta\omega_{\text{trial}}]$, centered about a universal average (or trial-averaged) frequency ω. These two types of jitter in the cycle length could be varied independently and had different effects on the oscillatory patterning observed in CCHs and ACHs (see below). In most simulations, all neurons received perfectly coherent (in-phase) rhythmic inhibition, which meant that, whereas the effective conductance strength g_i of the inhibitory current $I_i(t)$ could vary from neuron to neuron, the summated conductance profile $s_i(t)$ of the oscillation was identical for all neurons.

Stochastic fluctuations and offsets in gamma phase

In a specific set of simulations, we allowed for phase differences to occur in the cycles of the rhythmic inhibitory inputs to two different groups of neurons, instead of maintaining perfectly coherent oscillations. This offset was implemented by generating an additional set of fluctuations in the cycle length independently for each group. The onset times $T^1_{j,n+1}$ and $T^2_{j,n+1}$ of the $(n + 1)$th gamma cycle for neuron groups 1 and 2, respectively, were given by

$$T^1_{j,n+1} = T^1_{j,n} + \delta T^1_{j,n}, \quad T^2_{j,n+1} = T^2_{j,n} + \delta T^2_{j,n}$$

To generate $\delta T^1_{j,n}$ and $\delta T^2_{j,n}$, we then introduced jitter terms $\delta v^1_{j,n}$ and $\delta v^2_{j,n}$, which were sampled from a normal distribution with mean 0 and SD Δv_{trial}, along with a third jitter term $\delta\omega_{j,n}$, which was sampled from a normal distribution with mean 0 and SD $\Delta\omega_{\text{trial}}$, and set

$$\delta T^1_{j,n} = \frac{1000\,ms/s}{\omega_j + \delta\omega_{j,n} + \delta v^1_{j,n}}, \quad \delta T^2_{j,n} = \frac{1000\,ms/s}{\omega_j + \delta\omega_{j,n} + \delta v^2_{j,n}},$$

to produce two gamma oscillations with zero mean phase difference. Importantly, as $\delta\omega_{j,n}$, $\delta v^1_{j,n}$, and $\delta v^2_{j,n}$ all contributed to the jitter of the cycle length for each population, $\Delta\omega_{\text{trial}}$ could be decreased while Δv_{trial} was simultaneously increased to maintain the same degree of jitter to each group while increasing the average phase offset.

Results

To characterise the response properties of neurons that synchronise promiscuously with other cells, even when lacking a common orientation preference, we performed experimental recordings in cat area 17 during the presentation of oriented stimuli. Next, to test a possible mechanism that could account for our experimental findings, we simulated the activity of a collection of computational model neurons (see Materials and methods).

Experiment

Coherent gamma oscillations in cat area 17

Recordings from cat area 17 afforded an opportunity to examine various relations between autocorrelogram (ACH) and crosscorrelogram (CCH) characteristics and the orientation selectivity of the response to visual stimuli during gamma oscillations. MUA and SUA were recorded from many electrodes in parallel using two probes, each containing 16 channels, and analysed for each of 12 stimulus conditions (spanning orientations in increments of 30°; see Materials and methods). In total we obtained responses (MUA) from 94 recording sites in three cats, with 31 single units extracted from the MUA in one cat. Most MUA and SUA were selective for orientation, with corresponding tuning curves featuring a diversity of widths as shown in Figs 3B1 and C1. The majority of units exhibited oscillations in the gamma frequency band in their ACHs for a subset of the stimulus conditions, with the strongest oscillations typically arising at or near the optimal stimulus. Rastergrams of MUA (Figs 1A and B, thin tall lines) and SUA (Figs 1A and B, short thick lines), recorded at 10 contacts of a single probe for two stimulus directions, illustrate how tightly the windows of enhanced firing during the gamma cycles line up in time, which indicates a coherent oscillation across the probe. The locations of the recorded channels are highlighted by the dashed circles in Fig. 1C. The rastergrams also highlight the variability in the length of each gamma cycle as well as the duration of enhanced firing within each cycle. MUA and SUA generally showed strong similarities in synchrony and oscillatory patterning, as illustrated by the CCHs, ACHs, and orientation tuning curves shown in Fig. 1D. Due to the sparseness of the CCHs resulting from SUA data, we focused on the MUA in our subsequent analyses.

Sharply-tuned units that synchronise well exhibit strong oscillations at preferred orientations

As noted in the Introduction, we defined units in cat area 17 as SHs based on their synchronisation promiscuity, i.e. the tendency to synchronise strongly with other neurons regardless of orientation preferences. Synchronisation was generally graded across the units recorded by each probe and its range varied from probe to probe and from cat to cat, thereby making any designation of SHs rather arbitrary. Nevertheless, for concreteness in this study, we defined relative criteria for a unit to be an SH based upon both (i) its overall strength of synchronisation and (ii) the number of units recorded by the same probe that it synchronised with across all stimulus orientations. Specifically, a unit was classified as an SH if it exceeded two thresholds: (i) its synchrony strength (Materials and methods) computed with all units recorded by the same probe exceeded the average synchrony strength of all units recorded by the same probe, and (ii) its pairwise synchrony strengths computed with at least 8 of 16 individual units recorded by the same probe exceeded the average synchrony strength of all units recorded by the same probe. Generally, a unit's synchrony strength was positively correlated with the number of units that it synchronised strongly with. Units that satisfied criterion (i) but fell just short of criterion (ii) were considered moderate SHs and tended to synchronise strongly with other SHs. A total of 20 of 94 units were classified as SHs according to criteria (i) and (ii) (Cat 1: 5 of 30 units; Cat 2: 8 of 32 units; Cat 3: 7 of 32 units).

For example, unit 8, shown in Fig. 1D, was identified as an SH as it exhibited strong synchronisation with the activity in various other units over the range of stimulus directions; unit 3 was found to be a moderate SH with similar synchrony strength as unit 8 but it fell short of satisfying criterion (ii) with only seven other units (results not shown). Importantly, both units also exhibited strong oscillatory patterning in their ACHs as shown in Fig. 1D. An example of synchronisation promiscuity is illustrated in Fig. 2 based on two pairs of units, one composed of nSH 18 and SH 20 and the other consisting of nSH 25 and SH 28. The tuning curves in Fig. 2A (diagonal panels for each direction) indicate that the two pairs have different preferred orientations. Nevertheless, the strongest synchronisation occurs between the SHs and the weakest between the nSHs, as shown in Fig. 2B1 for these pairs of units and in Fig. 2B2–4 for other SH/nSH pairs. These results illustrate how the synchronisation promiscuity of SHs extends beyond units with common preferred stimulus directions.

We used two measures of synchrony (Amari, 2009; Roudi *et al.*, 2009), which we termed the synchrony strength and the coincidence measure, to analyse SH, and we found that both measures yielded analogous general results (compare Figs 3 and S4). However, of the two, the coincidence measure is uniquely suited to identify certain key features in the experimental data that are predicted by the model. (i) The synchrony strength is defined as Pearson's coefficient of correlation between spike trains and is given by numbers ranging from -1 to 1, where 1 indicates perfect positive correlation, -1 perfect negative correlation and 0 complete lack of correlation. Pearson's correlation coefficient is a standard, easily understood

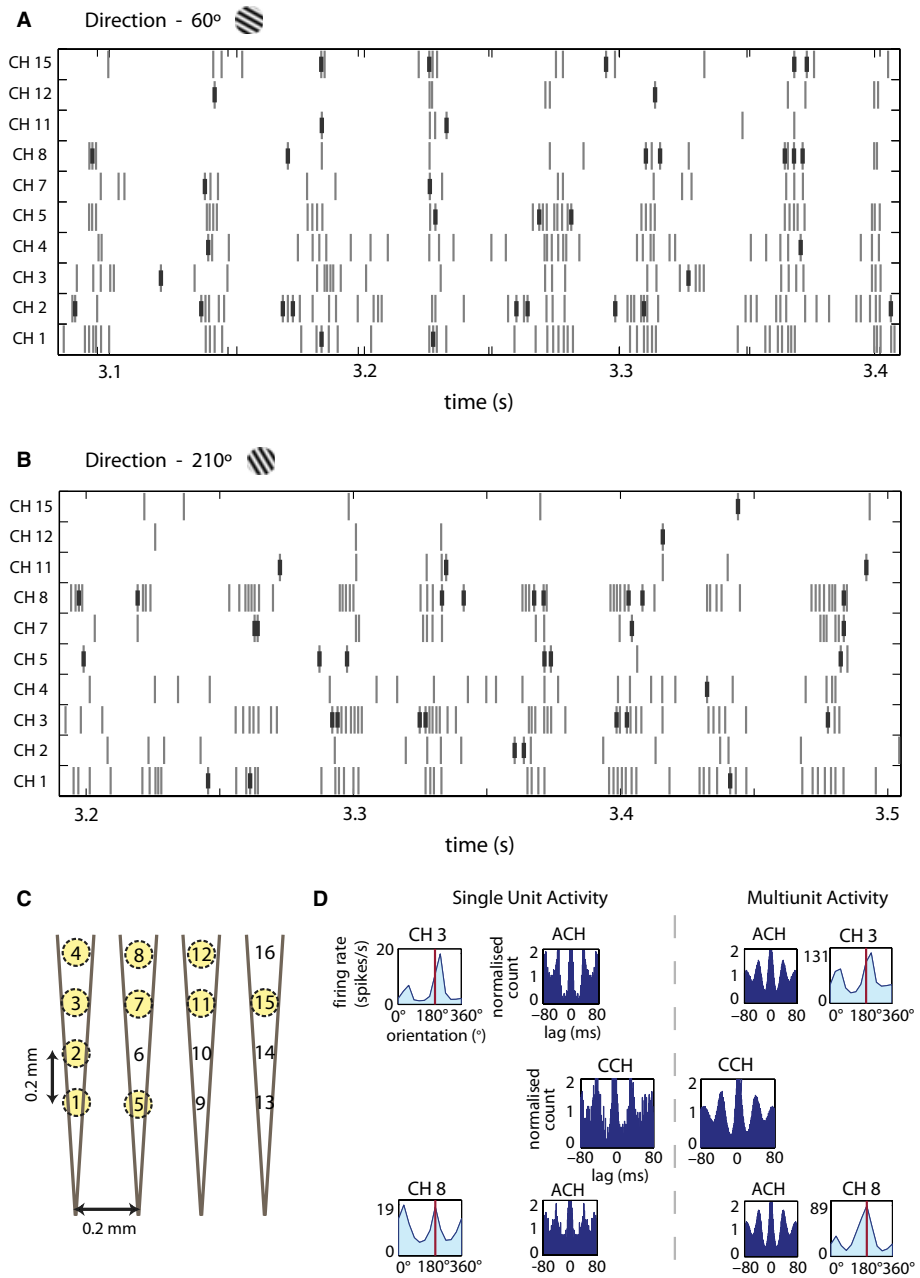

FIG. 1. Gamma oscillations in MUA and SUA recorded in parallel in cat area 17. For stimulus directions (A) 60° and (B) 210°, synchronous gamma oscillations are evident in rastergrams of parallel MUA and SUA observed within one probe. Thick black lines denote SUA and thin gray lines denote MUA. (C) The spatial distribution of the 16 channels (contacts) on probe 1 across a 0.6 × 0.6-mm patch of cat primary visual cortex; dashed circles indicate channels associated with the MUA in A and B. (D) A comparison of ACHs, CCHs (dark colored), and orientation tuning curves (light colored) for the SUA (left) and MUA (right) recorded in units 3 and 8 on probe 1 when the cells were stimulated nearly optimally (stimulus condition 210°, indicated by a vertical bar in each tuning curve).

measure of synchrony, allowing for comparison with results in other studies. However, a disadvantage of this measure for our particular purposes is that it scales the number of coincidences above baseline by the product of the SDs; therefore, it does not determine the percent increase in the number of coincidences above the baseline count expected based on the spike counts of the individual units. This can be relevant because spike counts differ from unit to unit and vary with stimulus orientation, particularly for MUA. Importantly, our computational model describes an underlying mechanism that increases synchrony by shaping the neuronal spiking in a manner that increases the percentage of coincident spikes above the baseline coincident count. (ii) The coincidence measure addresses these issues by directly computing the percent increase in the number of coincidences above baseline. Consequently, this method induces no biases towards favoring coincidences in high spike counts (high firing rates), and identical ratios between the CCH peak size and baseline are obtained irrespective of the average length of the empty time periods in the spike trains or the number of trains with only a few spikes in the trains. Thus, the values obtained from the coincidence measure are directly interpretable in terms of spike counts (and coincidence counts) irrespective of the variances within spike trains. Consistent with this description, two important features

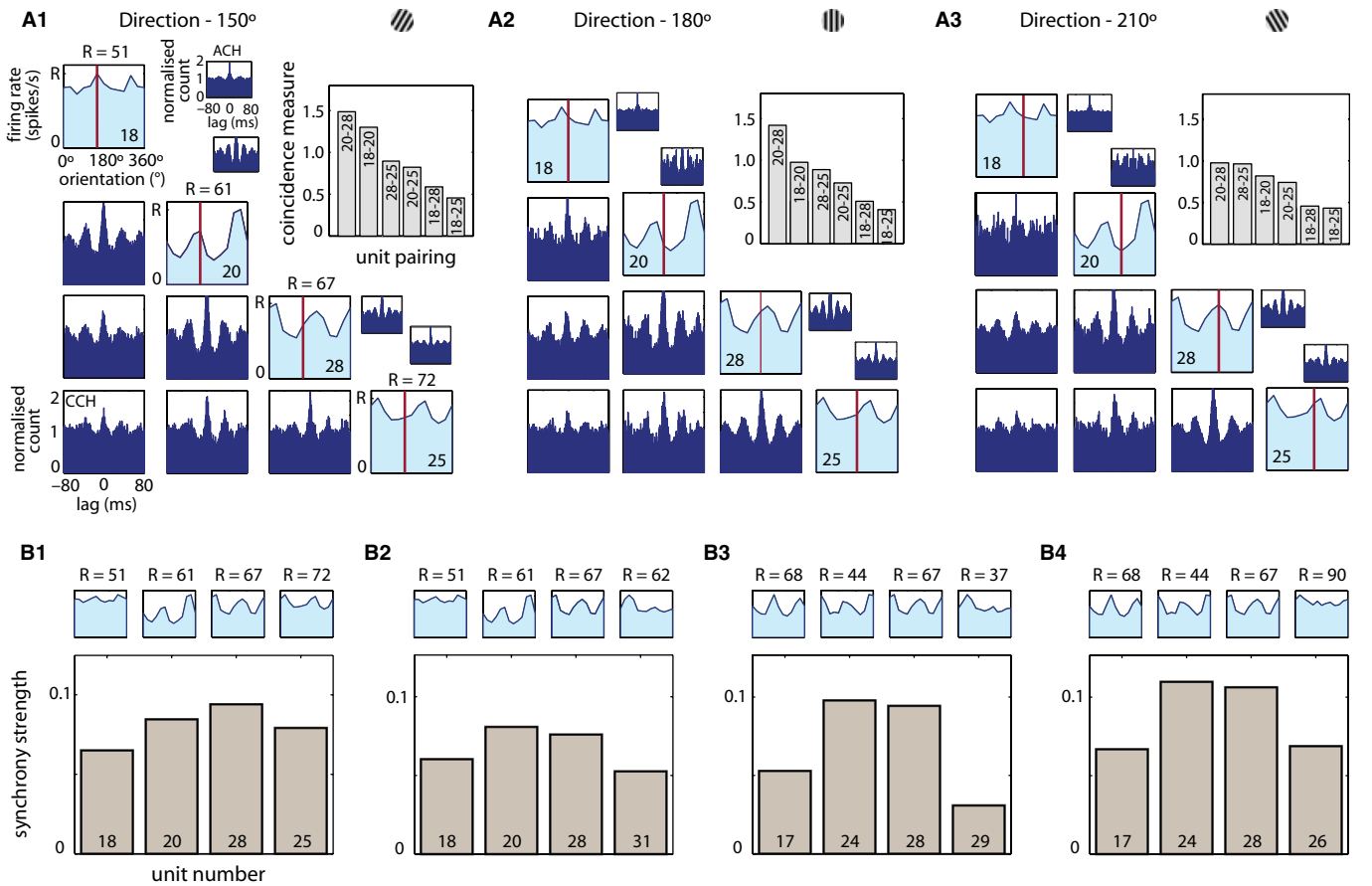

FIG. 2. SHs synchronise strongly across different stimulus conditions (single probe). (A) All panels show the ACHs and CCHs for the MUA recorded in four different units for three different stimulus directions. Along the diagonal of each panel, each unit is represented by its orientation tuning curve for the MUA (light colored), with the vertical line indicating the direction of the stimulus. Below the diagonal are CCHs computed between each pair of units, whereas ACHs for the units are shown above the diagonal (dark colored). For each stimulus direction, the insets show the coincidence measure for each pair of units (unit identities denoted by the pair of numbers in each bar), which indicates the relative increase in the number of coincidences above baseline. The units come from probe 2 and are arranged as pairs of units with similar orientation preferences within the pair, with a significant difference in preference between the pairs. Each pair is composed of a unit representing an SH (unit 20 or 28) and an nSH (unit 17 or 25). (B) Bar diagrams plotting the synchrony strength computed for analogous groupings of four units on probe 2 (Pearson's correlation coefficient averaged over the three pairwise interactions for each unit across all 12 stimulus directions); the middle pair in each panel, exhibiting increased synchrony strength in each case, are SHs. Plots above the bar diagrams show the corresponding orientation tuning curves for each unit. The left-most panel corresponds to the grouping of units in A.

in Fig. 2A that are identified using the coincidence measure and corresponding CCHs are that (i) the relative increase in coincidences above baseline was consistently the most pronounced between SHs; and (ii) the trend in the values of the coincidence measure between pairs of units also tended to correlate strongly with the trend in the oscillation strengths in the corresponding CCHs. In particular, the pair with highest percent increase in coincidences above baseline tended to be the pair with the strongest oscillations in the corresponding CCHs. These two distinct features of the experimental data are captured by our model.

The examples in Figs 1 and 2 also suggest a link between synchronisation promiscuity and oscillation strength in the gamma range. The SHs exhibited strong oscillations at the preferred stimulus directions (estimated by ACHs), as needed to allow the possibility of pronounced oscillations in the CCHs between the two SHs. In contrast, the oscillatory patterning was weakest for nSHs. Given the link between the tendency of a unit to synchronise promiscuously and the sharpness of its orientation tuning across all orientations (Yu *et al.*, 2008), we predicted that orientation selectivity would also positively correlate with the oscillation strength measured at the preferred orientation, where it tends to be maximal. In Fig. 3, we show two example multi-units, one highly selective for orientation (Fig. 3A1) and another with a moderate level of selectivity (Fig. 3A2), both from the same recording array (see Materials and methods). As predicted, the strongly selective unit exhibited more pronounced oscillations in the gamma range than the less selective one in response to the optimal stimulus for each unit.

Seeking to extrapolate from these examples, we examined whether the relationships among firing rates (orientation selectivity), amplitude of oscillations at the preferred orientation, and strength of synchronisation across a range of stimulus orientations are general. In Figs 3B and C, we show results pooled for a total of 62 MUAs across two recordings, each from a different cat. Although the two recordings showed different ranges in oscillation strength, synchrony strength, and orientation bias, we observed significant positive correlations between these features (Fig. 3). Also, the results were similar when synchrony strength was computed for the preferred orientation only (Fig. S1) or when scaled correlation analysis

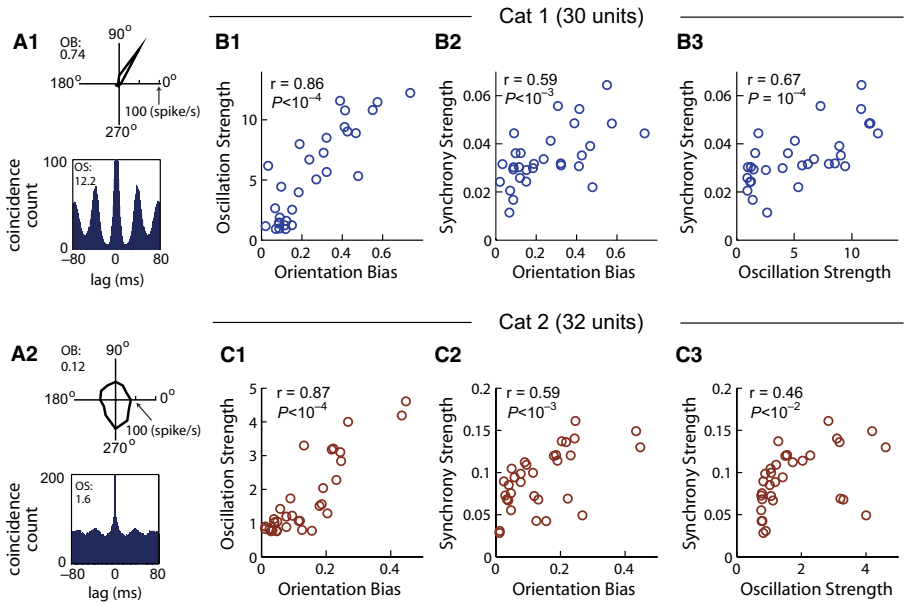

FIG. 3. Sharpness of orientation tuning, oscillation strength at preferred orientation, and synchrony strength across orientations are significantly correlated. (A1 and A2) Examples of data from two units (Cat 1), one strongly selective for the direction of the grating stimulus (A1) and the other moderately selective (A2). Top: tuning curves for 12 directions of drifting grating, shown as polar plots. Bottom: ACHs derived from responses to the most optimal stimulus. Orientation bias (OB) and oscillation score (OS) are indicated. (B and C) Pairwise plots relating strength of oscillation at preferred orientation (measured by the OS), synchrony strength, and orientation selectivity (measured by the OB) for a total of 62 units across two cats. Pearson's correlation coefficient *r* and the corresponding *P* value were calculated using the MATLAB function corrcoef. The *P* values indicate that the correlations are significant.

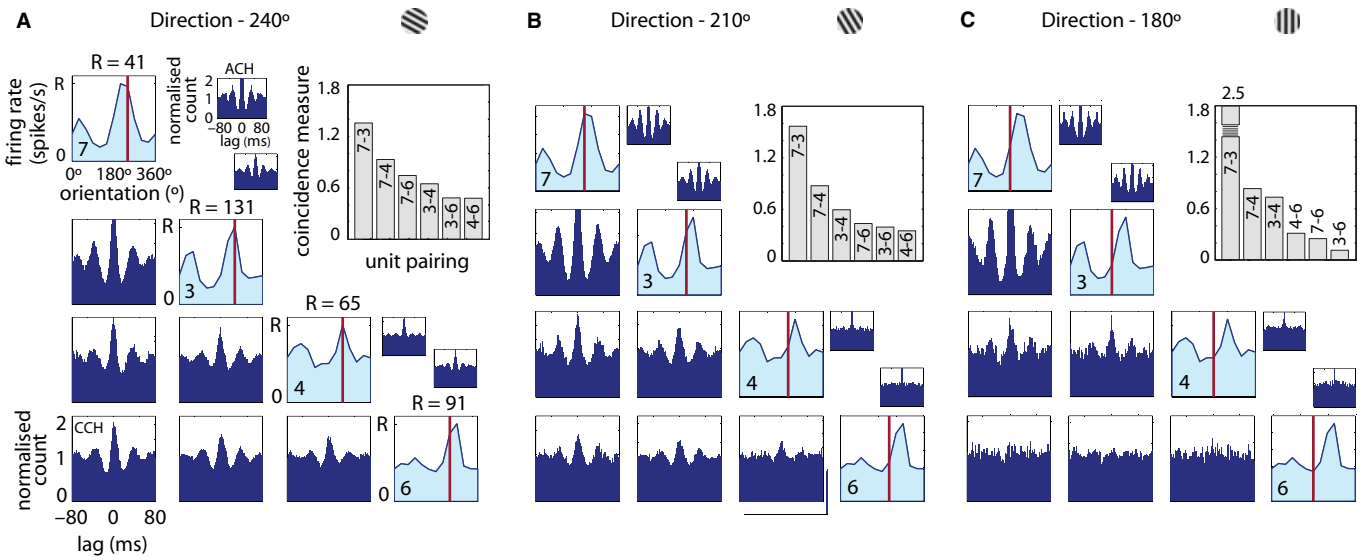

FIG. 4. SHs maintain oscillations strongly across different stimulus conditions shown in panels A-C (single probe). Figure layout is similar to that of Fig. 2A, however, the units come from probe 1, share a similar preferred orientation, and are ordered along the diagonal based on the strength of oscillations present in the ACHs (strongest to weakest).

was applied to exclude spurious effects of slow rate covariation (Fig. S2). To examine whether the positive correlations were merely a result of different numbers of SUA comprising the various MUA (e.g. MUA comprising larger numbers of SUA that have varying levels of orientation selectivity and oscillation strength could exhibit weaker orientation selectivity and oscillation strength than MUA composed of fewer SUA), we investigated how the correlations between orientation bias, oscillation strength, and synchrony strength change as a function of peak firing rates. In most cases, the peak firing rate did not affect the correlations (Fig. S3), suggesting that our results were not an artifact of MUA composition. Finally, analogous results to Fig. 3 were found when the coincidence measure was used in place of the synchrony strength (Fig. S4). Note that, although we have opted to categorise neurons as either SHs or nSHs, the borders of these categories are somewhat arbitrary as the neuronal response properties tend to be distributed along a continuum (Fig. 3), a feature that is reproduced by our computational model.

Synchronisation promiscuity and strong oscillations at non-preferred orientations

To compute the synchrony results shown in Fig. 3, we used the responses to all stimulus orientations to measure synchronisation promiscuity. Oscillation strength was computed using ACHs from preferred orientations only, as they tend to elicit the strongest oscillations and the high firing rate provides sufficient data to generate a well-resolved ACH for computing the oscillation strength. Moreover, measuring the oscillations at a single orientation avoids confounding the oscillation strength near its maximum value with the trend of oscillation strengths over the range of stimulus orientation. However, in considering the mechanisms underlying our data, we reasoned that synchronisation promiscuity may, in fact, be causally linked to the maintenance of strong oscillations away from preferred orientations. For example, in Fig. 2A, the units identified as SHs (units 20 and 28) maintained much stronger oscillations in their ACHs at non-optimal stimuli (150° for unit 20 and 210° for unit 28) than the other units. Thus, we next examined the link between synchronisation promiscuity and oscillation strength away from preferred orientations in our data.

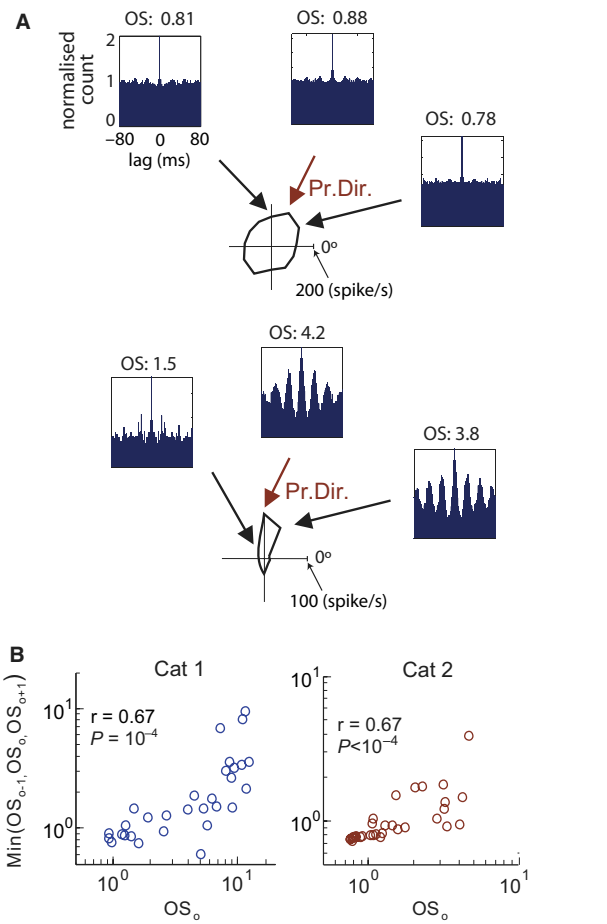

FIG. 5. Oscillation strengths in response to optimal and suboptimal stimuli are correlated. (A) Examples of two units (Cat 2), one with a weak oscillatory response to the optimal direction (Pr. Dir.) of the grating stimulus and the other with a strong oscillatory response. Orientation tuning curves (polar plots) and ACHs in response to both the optimal (light-colored arrow) and two suboptimal (black arrows) stimuli are shown. (B) The minimal oscillation scores (OSs) for the optimal (OS_o) and two suboptimal (30° away from the optimal directions; OS_{o+1} and OS_{o-1}) directions are plotted against the OS for the optimal direction (OS_o) for a total of 62 units, across two cats. A double-logarithmic scale is used in the scatter plots to increase the visual clarity.

Figure 4 illustrates another example showing that units that oscillate strongly at their preferred direction also maintain the strongest oscillations away from this direction. Tuning curves of four units with a common preferred orientation are arranged in order of decreasing oscillation strength at the preferred stimulus direction; the same order of oscillation strength is preserved across all three of the stimuli shown (i.e. the strongest oscillations are in unit 7 and the weakest in unit 6). The corresponding ACHs, CCHs, and coincidence measures demonstrate that, although the relative increase in the coincident spike count above baseline can vary markedly depending on stimulus direction, the largest numbers of coincidences relative to baseline and the strongest oscillations for all conditions occur for SHs and moderate SHs (units 7 and 3, respectively) and the weakest for nSHs (units 6 and 4). Note that the gamma-band oscillations in unit 6 are considerably diminished at direction 180°, coinciding with a drastic loss of synchrony with the other units. We also observed a sharper drop in firing rates associated with units 7 and 3 as stimulus direction was varied from 240° than in the firing rates of the other units (Fig. 4), consistent with earlier results (Yu *et al.*, 2008).

These examples of the persistence of relative oscillation strength across orientations were reproduced throughout our data. Figure 5A provides two examples of ACHs computed across multiple orientations, one set from a broadly tuned unit exhibiting weak oscillations at the preferred orientation and the two adjacent orientations, and another set from a sharply tuned unit that maintains strong oscillations at analogous orientations. In our pooled results of 62 MUAs shown in Fig. 5B, we found a significant positive correlation between the oscillation strength arising at a unit's preferred orientation and the minimal oscillation strength measured across the preferred and two adjacent orientations (e.g. Fig. 5A), indicating that strongly oscillatory units maintained strong oscillations away from their preferred orientations (Fig. 5B).

Synchrony between probes

The definition of our synchrony measure implies that the synchrony between two units exhibiting strong oscillations will be strong if their oscillations are coherent. Consequently, we reasoned that the strength of synchronisation over long distances (between two probes) would depend strongly on the presence of coherent oscillations in the gamma band across the two locations. CCHs computed between units in two different probes separated by at least 1 mm generally showed significantly shorter (or non-existent) central peaks and weaker oscillations, relative to the CCHs found within a single probe (0.6 × 0.6 mm). This result is consistent with earlier work on carbachol-induced gamma oscillations in slices from the entorhinal cortex, in which the strength of synchronisation at multiple recording sites declined with increasing spatial distance between electrodes (Dickson *et al.*, 2000). We also found that synchronisation across probes was restricted to a narrower range of stimulus conditions when compared with units recorded by a single probe.

We did, however, find several cases of strong synchrony and oscillatory CCHs over long distances. These cases occurred exclusively for SHs and moderate SHs. Figure 6A shows examples for two pairs of units. All four units show strong oscillations for stimulus direction 180°. The reduction in oscillation strength for stimuli at 210°, and further drop at 240°, is associated with a much more dramatic decline of long-distance synchronisation between the two probes, such that synchrony is not even detectable in the CCHs at 240°. In Fig. 6B, we plot representative examples of rastergrams for 500-ms recordings (MUA) in response to two different stimulus directions. Windows of enhanced

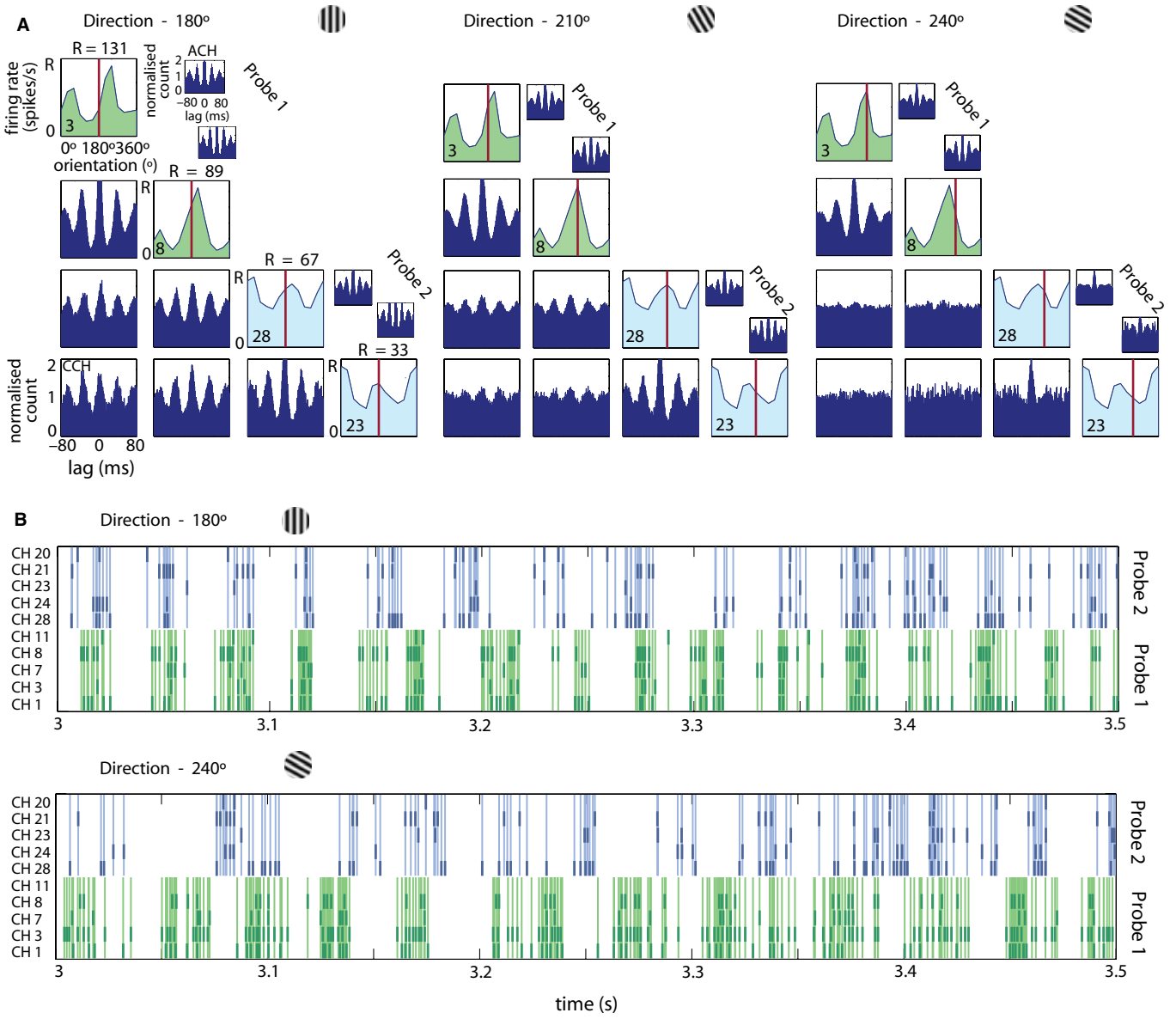

FIG. 6. Synchronisation between two probes relates to coherent oscillations in the gamma band. (A) ACHs, CCHs, and orientation tuning curves for four units, two from probe 1 (dark-colored tuning curves) and two from probe 2 (light-colored tuning curves). All four units have strong oscillations in their ACHs for at least one stimulus direction and were categorised as SHs (units 8 and 28) or moderate SHs (units 3 and 23). (B) Rastergrams for 10 units from two probes for the same trial. The dark-colored short lines in each row represent the spike times of the MUA recorded in each unit. Each short line is extended into a light-colored line to help visualisation of the cycles of the gamma oscillations at respective probes.

firing across the two probes align more often for the stimulus direction that produces overall stronger oscillations (more often for 180° than for 240°). This comparison supports the notion that the significant increase in coincident firing relative to baseline, indicated by the center peak heights in the CCHs between units in two different probes, is closely tied to the degree to which the oscillatory firing patterns are in phase across distant recording sites.

Simulations

Hypothesised mechanism for synchronisation hubs

Activity in networks of inhibitory neurons has been strongly linked to the generation of gamma oscillations through experiments on *in vitro* slice preparations pharmacologically treated with kainate and/or carbachol (Whittington *et al.*, 1995; Buhl *et al.*, 1998; Fisahn *et al.*, 1998; Dickson *et al.*, 2000; Traub *et al.*, 2000; Whittington *et al.*, 2000; Cunningham *et al.*, 2003; Traub *et al.*, 2005) and through computational studies (Van Vreeswijk *et al.*, 1994; Traub *et al.*, 1996; Wang & Buzsaki, 1996; White *et al.*, 1998; Traub *et al.*, 2000; Tiesinga *et al.*, 2001; Börgers & Kopell, 2003; Doiron *et al.*, 2003; Bartos *et al.*, 2007). Gamma rhythmicity is evident in inhibitory postsynaptic potentials recorded in the cat visual cortex (Ferster, 1986), and rhythmic inhibitory postsynaptic potentials help control the probability and timing of pyramidal cell spikes during gamma oscillations (Csicsvari *et al.*, 2003; Hasenstaub *et al.*, 2005). Further evidence for the involvement of inhibitory interneurons in gamma oscillations *in vivo* is demonstrated through recent experiments conducted using optogenetics (Cardin *et al.*, 2009; Sohal *et al.*, 2009). We hypothesised that a single property, heterogeneity

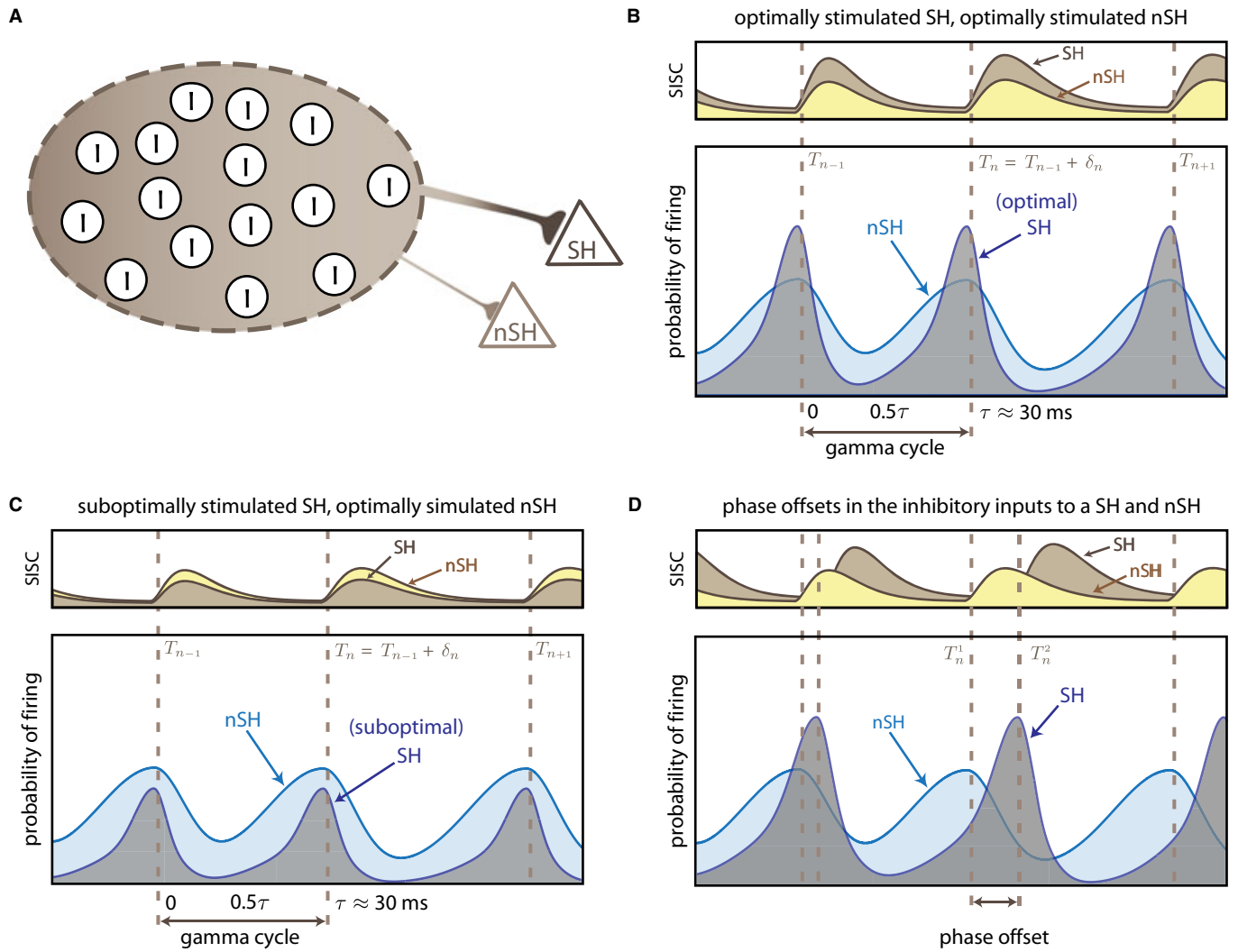

FIG. 7. Schematic illustration of how rhythmic inhibition may shape excitatory neuron firing at different phases of the gamma cycle. (A) A pool of inhibitory interneurons engaging in synchronous oscillations delivers approximately synchronous (i.e. narrowly distributed) pulses of synaptic inhibition to excitatory neurons. In our model, SHs receive stronger levels of rhythmic inhibition from the inhibitory pool compared with neurons that are nSHs as represented here by connection thicknesses. (B–D) Cumulative or summated inhibitory synaptic conductance (SISC) from the pool of interneurons (top) arrives in rhythmic pulses in the gamma frequency range, with SHs receiving a larger signal compared with nSHs, resulting in a qualitative difference in the probability of excitatory neuron firing across the phases of the gamma cycle (bottom). (B) When an SH and nSH are both optimally stimulated, the SH receives a larger SISC than the nSH. Although this disparity results in significant differences in the neurons' probabilities of firing, the oscillatory inputs to the two neurons are perfectly in phase, resulting in direct overlap of their windows of maximal firing, which promotes synchrony. (C) A suboptimally stimulated SH receives relatively weak inhibition (SISC) balanced by relative weak excitation to maintain a relatively narrow window of maximal firing that still promotes synchronisation with an optimally stimulated nSH. (D) Analogous plots to B with phase offsets introduced between the oscillations for two different excitatory neurons, which results in less overlap in the phases of maximal firing for the two neurons during each cycle.

in the strength and tuning of gamma-modulated inhibition to different excitatory neurons, could be predominantly responsible for the covariation among oscillation strength at preferred and non-preferred orientations, synchronisation promiscuity, and orientation tuning that we observed in cat area 17. In particular, SHs would be those neurons receiving the strongest inhibition. To test the feasibility of this hypothesis, we simulated a model consisting of a small set of excitatory neurons that were not directly connected and that received independent, Poisson-distributed excitatory inputs as well as inhibitory inputs correlated through a shared rhythm.

The schematic diagrams in Fig. 7 illustrate our proposed mechanism for the origin of SHs. Although there may be a continuum of strengths of rhythmic synaptic inhibition received by different neurons, the illustration in Fig. 7A compares two levels of inhibition, figuratively representing inputs to an SH and to an nSH. Although inhibition does not directly induce spiking, we conjectured that the stronger inhibition to the SH would cause its firing to be more tightly constrained in time as illustrated in Fig. 7B. In particular, the effect of inhibition could be strong enough to constrain firing in this way even though the SH would also receive stronger excitation than the nSH to maintain similar firing rates of the SH and nSH at their preferred orientations, in agreement with experimental recordings (Nikolić, 2009). We used simulations of the computational model to explore the extent to which such shaping of activity by rhythmic synaptic inhibition could arise and could control synchronisation promiscuity in conjunction with oscillation strength and orientation tuning. Moreover, we reasoned that the strength of synchronisation measured between two neurons would also depend on the degree to

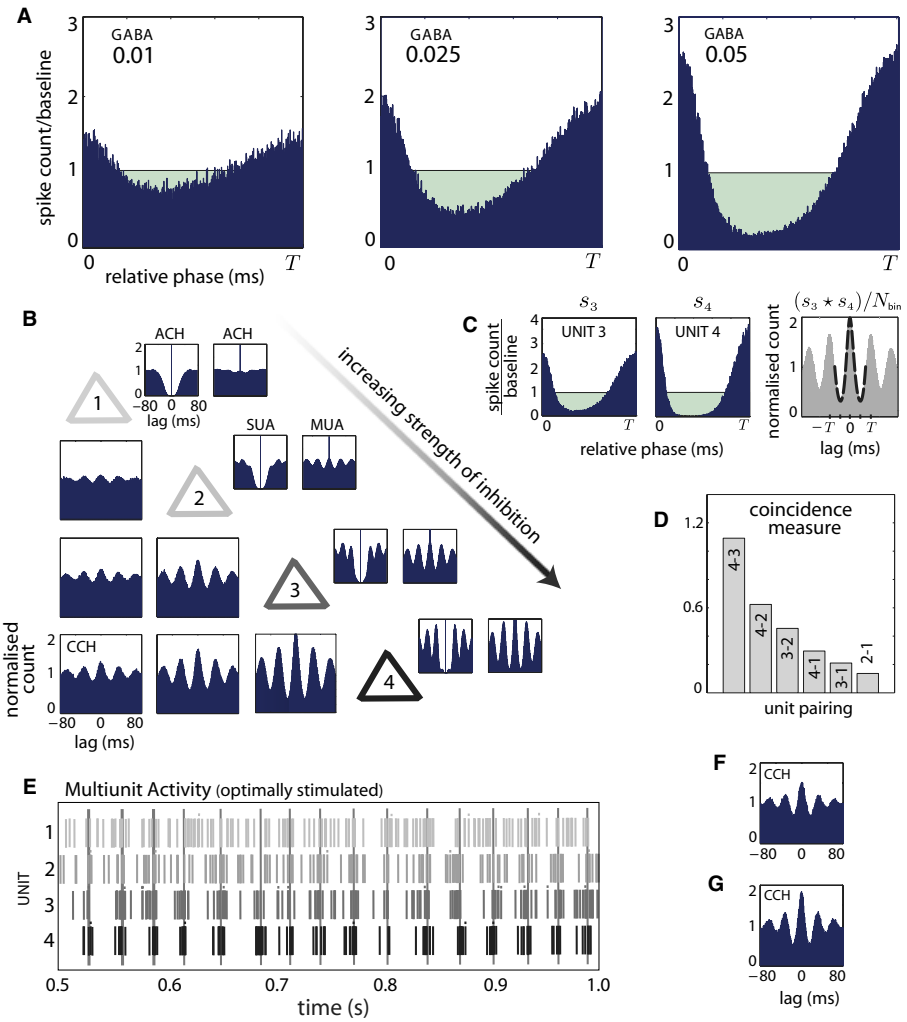

FIG. 8. Rhythmic inhibitory input shapes the timing of neuronal firing. Results of simulations with integrate-and-fire neurons are shown. In all cases, neurons are optimally stimulated, represented by a tuning of inputs to elicit an average firing rate of 10 spikes/s. (A) Histograms of spike counts at different phases (computed by partitioning the average cycle length T into $N_{\text{bin}} = 500$ bins) during inhibitory gamma oscillations of three different strengths (left, $g_i = 0.01$ mS/cm^2; center, $g_i = 0.025$ mS/cm^2; right, $g_i = 0.05$ mS/cm^2), normalised by the baseline spike count computed in the absence of inhibition (also shown as light-colored background). The differences relative to baseline reveal a window of enhanced firing toward the end of the gamma cycle, when inhibition is attenuated. (B) Autocorrelograms (ACHs) (above diagonal) and crosscorrelograms (CCHs) (below diagonal) for four excitatory neurons subject to different levels of coherent rhythmic inhibition (neuron 1, $g_i = 0.01$ mS/cm^2; neuron 2, $g_i = 0.025$ mS/cm^2; neuron 3, $g_i = 0.05$ mS/cm^2; neuron 4, $g_i = 0.1$ mS/cm^2). In each plot, the vertical axis denotes the total number of coincidences normalised by the baseline number of coincidences, and the horizontal axis denotes the lag (in ms). ACHs were computed for simulated SUA (left) and MUA (right). Increasing levels of inhibition and concomitant excitation to maintain a rate of 10 spikes/s result in stronger oscillations in the ACHs and CCHs and stronger synchrony, indicated by taller central peaks in the CCHs. (C) Left and middle: plot of the normalised spike count histograms s_3 and s_4 computed for unit 3 ($g_i = 0.05$ mS/cm^2) and unit 4 ($g_i = 0.01$ mS/cm^2), respectively, at different phases of the gamma oscillation (as shown in A). Right: crosscorrelation $(s_3 \star s_4)/N_{\text{bin}}$ (dashed curve) overlaid with the CCH (gray histogram) from B computed between units 3 and 4. The strong agreement between the central peaks and adjacent troughs of each indicates that the pronounced center peak in the CCH is predominantly generated by the overlap in windows of enhanced firing at the end of each gamma cycle in the two units. (D) The coincidence measure (Materials and methods) computed for each of the six CCHs in B indicates that stronger, coherent rhythmic inhibition yields an increase in the number of coincidences relative to the baseline number of coincidences. (E) Rastergrams of simulated SUA (dots) and MUA (bars) for four levels of rhythmic coherent inhibition matching the levels used for neurons 1–4 in B. Each neuron has the same average firing rate, and an increase in input strength results in a narrowing of the window of enhanced firing at the end of the gamma cycle (each onset of a gamma cycle is indicated by a vertical line). CCH for a pair of neurons with the same average firing rate, receiving the same level of rhythmic inhibition, with synaptic excitation to the neurons generated stochastically by a homogeneous Poisson process only (F) or by a combination of a homogeneous Poisson process and a non-homogeneous, gamma-modulated Poisson process (G).

which their oscillatory inhibitory inputs were coherent and how they varied across cycles or trials (Fig. 7C), and thus we also explored these effects computationally.

Rhythmic inhibition determines spike patterning and synchrony

Simulations were performed with integrate-and-fire and conductance-based model neurons (see Materials and methods). In these simulations, in addition to coherent rhythmic inhibition oscillating in the gamma frequency range, the excitatory neurons were subject to excitatory input with some rate fluctuations (Materials and methods). We assumed that all neurons fired at the same rate when optimally stimulated and that they exhibited a tuned response, with average firing rates varying depending on the optimality of a hypothetical presented stimulus; we varied the strengths of inhibition and excitation to provide a representation of stimulus optimality.

For each neuron in this particular set of simulations, we generated a cycle-averaged histogram of normalised spike counts at different phases of the rhythmic inhibition cycle for different inhibition strengths (defined in terms of both the number and efficacy of synaptic inputs producing it) (Fig. 8A). The normalised spike counts were calculated as follows. After each simulation was completed, we rescaled each cycle length to match the trial-averaged cycle length $T = \omega^{-1}(1000 \text{ ms/s})$ and converted the time within a cycle to the relative phase (between 0 at the beginning of the cycle and T at the end of the normalised cycle). Histograms of spike counts, as a function of relative phase, were then computed by averaging over trials and dividing by the average number of cycles; for a histogram with $k = 500$ bins (each corresponding to a phase range of $T/k = 0.002T$), the value corresponding to the first bin was the average number of spikes during each cycle that occurred between phase 0 and phase T/k during each cycle, the second bin displayed the average number of spikes between phase T/k and phase $2T/k$, and so on. As a baseline case, we also performed a simulation in the absence of inhibition in which excitatory inputs were generated by a homogeneous Poisson process. The elapsed time during the baseline simulation was partitioned into cycles of the same time lengths used for the simulations with inhibition, cycles were rescaled to units of phase, and a baseline spike count for each phase bin was computed by averaging over all cycles. Due to the Poisson inputs, the probability of firing at each phase in the baseline simulations was equal, and the resulting uniform baseline spike count was used to normalise the spike counts obtained with inhibition.

In Fig. 8A, deviations from the baseline count indicate regions of increased or decreased spike counts, on average, during each cycle of the gamma oscillation. As the level of rhythmic inhibition increases, it shapes more drastically the timing of the firing output of the excitatory neuron despite concomitant adjustments of excitation levels to maintain a constant firing rate (Fig. 7). Consistent with this result, ACHs for single model neurons and for simulated MUA accumulated over many trials (each tens of seconds in length) exhibit a graded increase in the strength of oscillations in the (constant rate) firing output as the strength of rhythmic inhibition increases, as shown in Fig. 8B. The six CCHs computed for all possible pairs among the four units also show an inhibition-dependent increase in oscillation strength (Fig. 8B). Importantly, as indicated by the growing height of the central peak in the normalised CCHs, the number of coincident spikes measured above baseline increases from neurons 1–2, with the weakest levels of inhibition, to neurons 3–4, with the strongest levels of inhibition. This trend is quantified by the coincidence measure plotted in Fig. 8D, which is computed pairwise between the four neurons.

Given that the average firing rate remains constant for the different levels of inhibitory input, the high concentration of spikes in narrow windows that occurs for higher levels of inhibition (as in the histograms in Fig. 8A) reflects the expected increase in the probability of firing towards the end of each gamma cycle. The overlap of these windows of elevated firing can then be related to the probability of coincident spikes between neurons (see Appendix), providing an explanation of how strong rhythmic inhibition in the model can serve both to produce stronger oscillations in the firing output and increase the probability of coincident spikes. Indeed, as can be seen in Fig. 8C, the correlation function computed from the normalised cycle-averaged spike histograms (in Fig. 8A) for any two neurons closely matches the center peak of the normalised CCH (which measures actual coincidences) between those neurons. As the spike histograms and CCHs are calculated relative to baseline, modulations to the synchrony strength arising from differences in average firing rates are effectively scaled out, thereby (i) directly identifying the relative increase in coincident spikes (above baseline) that result from the shaping of the firing windows, e.g. by rhythmic inhibition, and (ii) allowing for a more direct comparison between pairings of neurons with different firing rates.

The shaping of the firing output by rhythmic inhibition is also evident in rastergrams of simulated MUA, each composed of 15 independent neurons subject to inhibitory input with the same rhythmic time course at the same strength (Fig. 8E). This shaping of firing times provides a primary mechanism that underlies both the oscillations and synchrony in the ACHs and CCHs that we observe. Note that the ACHs and CCHs computed from our simulations exhibit attenuation away from their central peaks, analogous to those seen in ACHs and CCHs calculated from experimental data, due to fluctuations in the cycle lengths of the rhythmic inhibition (see Supporting Information Results, Fig. S5 and Materials and methods).

These effects of inhibition on spike timing are further enhanced by the inclusion of a gamma-modulated stochastic component of the excitatory synaptic input (e.g. representing output of excitatory neurons in the cortical layer that are subject to gamma inhibition). This enhancement is illustrated by comparing the CCHs between a pair of neurons in two cases, shown in Fig. 8F and G. The inhibitory input strength and firing rates are the same in both cases, but in one the excitatory input is generated by a homogeneous Poisson process only (Fig. 8F), and in the other it consists of a mixture of a homogeneous Poisson stream and a gamma-modulated excitatory component (Fig. 8G). The gamma-modulated component yields stronger oscillations in the CCH with a larger central peak, as this component also plays a role in shaping the firing window; however, at stronger levels of inhibition (and correspondingly higher levels of excitation), the effect that increasing the gamma-modulated component has on shaping the firing window becomes less pronounced unless the rhythmic excitatory input is further constrained to increasingly narrow windows.

Hubs coordinated by strong, coherent inhibition synchronise promiscuously

Based on the output patterning described above, we hypothesised that the strength of a rhythmic inhibitory signal to a neuron could control the promiscuity with which it synchronises with other neurons that also receive in-phase rhythmic inhibition but do not necessarily share its orientation preference. To investigate this idea, we considered model neurons with simulated orientation tuning. This tuned response was achieved by jointly varying the strengths of rhythmic inhibitory, rhythmic excitatory, and homogeneous Poisson excitatory inputs to these neurons to represent varying degrees of stimulus optimality (with 10 spikes/s activity at fully optimal stimulation). Certain neurons were selected to receive inhibition at twice the strength of the inhibition to the other neurons sharing their stimulus preferences, with excitation scaled accordingly to maintain equal firing rates. Simulations showed that these strongly inhibited neurons consistently exhibited the highest degree of synchronisation and the highest rate of spike coincidences above baseline with other neurons. Consequently, we labeled these as SHs and denoted the other weakly synchronising neurons as nSHs.

Next, we considered a set of four model neurons organised in two pairs. Each pair consisted of an SH and an nSH. Neurons within a pair were assumed to have the same stimulus preference. In one case, both pairs of neurons were stimulated optimally and in another case one pair of neurons was stimulated optimally and the other suboptimally. The stronger rhythmic inhibition to the SHs was

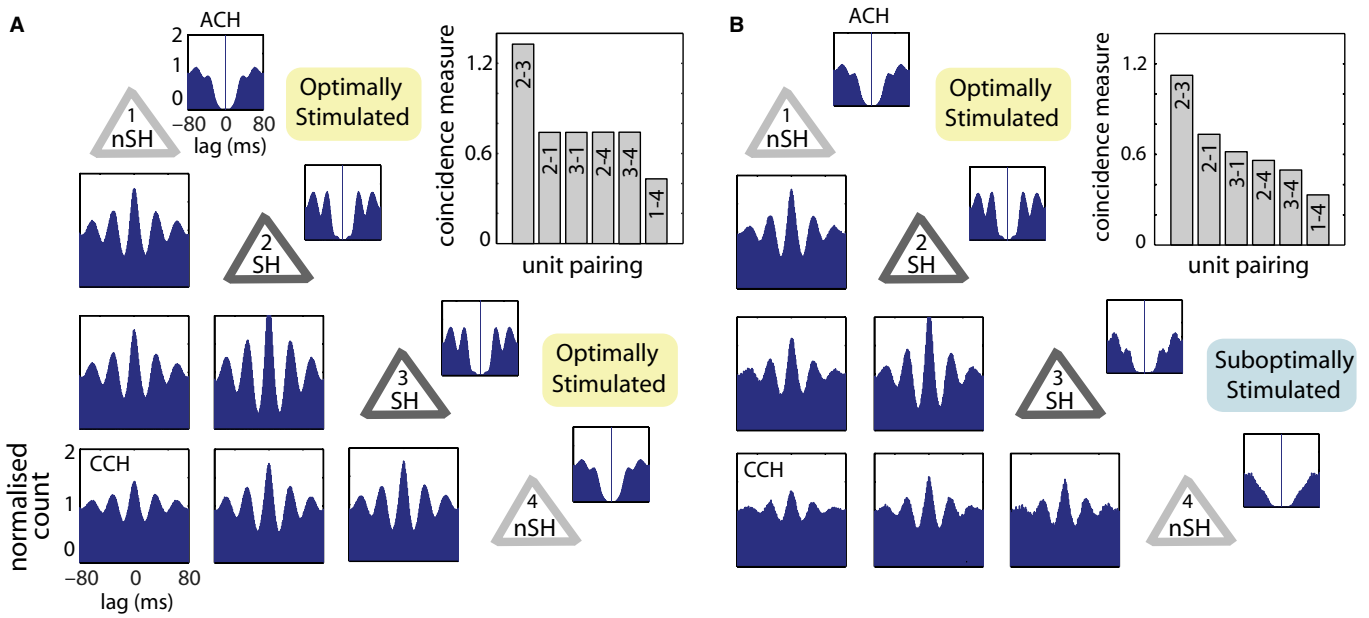

FIG. 9. Graded synchronisation between SHs and nSHs. (A) Oscillatory patterning is evident in CCHs and ACHs computed for four neurons grouped into two pairs, each composed of an SH and an nSH that are optimally stimulated, all with an average firing rate of 10 spikes/s. The vertical axes of the ACH/CCHs represent the total number of coincidences normalised by the baseline number of coincidences for different time lags, and the time lag along the horizontal axis is measured in 1-ms bins. The inset shows a bar diagram of the coincidence measure computed from each of the CCHs, where the pair of numbers in each bar corresponds to the numbers used to label the neurons in the diagonal of the main figure. (B) When one pair of neurons is suboptimally stimulated, achieved by weakening inputs to elicit an average firing rate of 3–4 spikes/s, the oscillations in the neurons' ACHs are suppressed. Nonetheless, oscillations remain in the CCHs, particularly those involving either or both SHs. The coincidence measure becomes graded, with substantially more coincidences above baseline in pairs involving at least one SH than in the nSH–nSH pair (inset).

reflected in the enhanced strength of oscillations in their ACHs relative to those of the nSHs (Fig. 9). Because of the strong inhibition to SHs, some ACH patterning persisted even with the weakening of inputs associated with a non-optimal stimulus (Fig. 9B). In both the optimal–optimal (Fig. 9A) and the optimal–suboptimal (Fig. 9B) cases, the largest value of the coincidence measure occurred between the two SHs (neurons 2 and 3), indicating that neurons subject to the strongest levels of rhythmic inhibition exhibited the largest increase in coincident spikes above baseline. The weakest value of the coincidence measure was always found between the two nSHs. All results were consistent with the SH and nSH labels; all CCHs and coincidence measures involving at least one SH showed a significantly greater number of coincidences relative to baseline than the case of the nSH–nSH. With only optimal stimulation, the four SH–nSH pairings had similar CCHs and coincidence measures (Fig. 9A), whereas the values of the coincidence measure for the SH–nSH pairings became more graded when the stimulus to one pair was made non-optimal (Fig. 9B). A key point in explaining these results is that, although the inhibitory and excitatory oscillatory inputs to each neuron differ in strength from those to all three

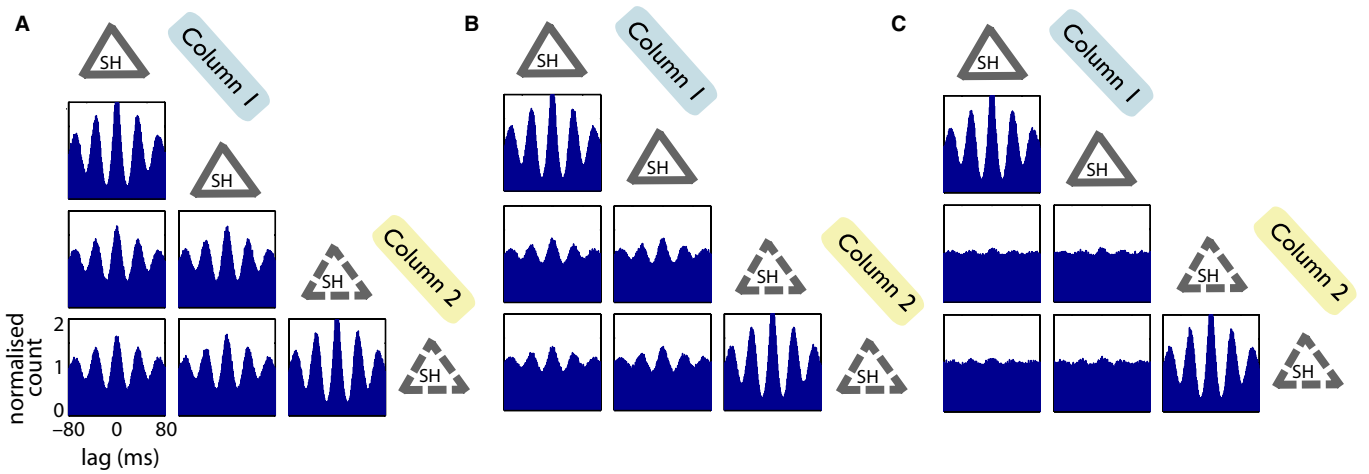

FIG. 10. Loss of gamma coherence leads to a rapid decrease in synchrony. Each panel shows the CCHs between four SHs grouped into two pairs, each considered as corresponding to its own cortical column. A pair of neurons within the same column receives perfectly coherent rhythmic inhibitory input; however, the phases of the rhythmic inputs in one column are offset relative to the inputs of the other column, in a way that varies stochastically from cycle to cycle. The size of the maximal offsets introduced on each cycle increases across panels from (A) 0.5 ms to (B) 1 ms to (C) 2 ms. An increase in phase offsets results in a substantial erosion of the central peak and strength of oscillations in the CCHs of pairs of neurons from two different columns.

other neurons, these inputs are perfectly coherent across all four neurons. Thus, although the rhythmic inputs are unable to induce strong oscillations in the ACHs of nSHs, the oscillations in SH firing translate into oscillations in the CCHs computed between the SHs and nSHs.

Although gamma oscillations may be in phase locally, our experimental results suggest that gamma oscillations between pairs of simultaneously recorded neurons that are separated by longer distances may become significantly less coherent (Fig. 6). We used independent jitter values to produce less coherent oscillations between two groups (columns) of model neurons (see Materials and methods), with each group receiving perfectly in-phase rhythmic inputs. With even fairly small increases in the size of the jitter, the central peak and the strength of oscillations in the CCHs between groups decayed significantly, as illustrated in Fig. 10. Importantly, this effect demonstrates that synchrony can be very sensitive to the degree to which the gamma oscillations are coherent across two columns. Moreover, it makes the prediction that, in experimental recordings, the windows of enhanced firing in two different probes should occur at similar phases when they exhibit strong synchrony and should become increasingly out of phase when synchrony is observed to weaken.

Oscillation strength and tuning curve sharpness

Our experimental results showed a covariation of oscillation strength and orientation selectivity (Fig. 3). In a final set of simulations, we addressed the relationship between oscillations and orientation tuning indirectly by differentially decreasing synaptic input parameters (g_i, r_{non}), from most to least optimal (in terms of ability to elicit spikes), in four steps denoted by stimulus conditions 0, 1, 2 and 3, respectively (Fig. 11A). Three different regimes of parameter reduction were considered. In two of these, all inputs were weakened proportionally to maintain the balance between excitation and inhibition (Mariño *et al.*, 2005; Isaacson & Scanziani, 2011), resulting in similar firing rates across regimes despite different input strengths (Fig. 11, solid lines). Both cases produced oscillations, but the case with stronger inhibition across all conditions (black) yielded significantly stronger oscillations. In the third regime, the inputs remained strong, but excitation declined more rapidly than inhibition (dashed black line) and the sharpest tuning and the strongest oscillations resulted. Here, the dominant inhibition effectively restricted spikes to windows of sufficient inhibitory decay for the suboptimal stimuli, curtailing firing rates and promoting oscillations. Thus, within this framework, relatively strong inhibition across all stimulation conditions appears to be critical for the empirically observed association between sharpness of orientation tuning and oscillation propensity.

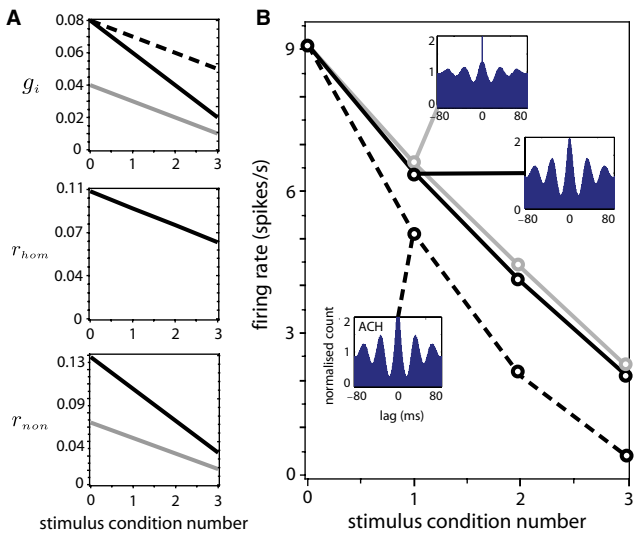

FIG. 11. Variation of inhibition and excitation modulates firing rate and oscillatory patterning. (A) Top: Strength of inhibition (g_i); middle: rate (r_{hom}) of homogeneous Poisson excitatory synaptic input; and bottom: rate (r_{non}) of gamma-modulated excitatory synaptic input. Three different sets of simulations were performed (solid gray, solid black, dashed black lines), each across four conditions (0, 1, 2, 3) corresponding to the decreasing trend of firing rates along an orientation tuning curve from the preferred orientation (Condition 0) through three successive suboptimal stimulus conditions (Conditions 1–3). As all three sets used the same level of r_{hom}, only one line is visible in the middle panel. The cases represented by the dashed and solid black lines also used the same level of r_{non}, shown by the solid black line in the bottom panel. In the cases marked with solid lines, excitation and inhibition were varied with slopes given by the same fixed proportion of maximal input magnitude. (B) Plot of the average firing rate computed for each set of inputs (firing rate curve lines are matched to those for the inputs), across all four conditions. Insets show ACHs for MUA for stimulus condition 1.

Discussion

Our experimental recordings during gamma oscillations in cat area 17 reveal a large degree of variability in the strength of oscillations, level of synchronisation, and sharpness of orientation selectivity across units recorded in parallel, and, furthermore, reveal that these three features are positively correlated. Units that exhibited particularly high synchronisation propensity, even across non-preferred stimulus orientations, we have dubbed SHs [in contrast to the 'hub cells' defined by Bonifazi *et al.* (2009), which are defined specifically in terms of their high connectivity and ability to strongly influence network dynamics, the term 'synchronisation hub' only requires the proclivity to synchronise with many neurons, irrespective of their afferent connections and influence]. Such units also typically exhibited strong oscillations and sharp tuning curves. Using a computational model, we demonstrate that rhythmic synaptic inhibition that is relatively coherent over the spatial extent of a probe (< 0.6–0.84 mm) might lie at the heart of these relationships. In particular, three facets of the synaptic inhibition to a neuron during gamma oscillations, namely its strength, its rhythmicity, and the extent to which it is in phase across different neurons, play critical roles in determining the neuron's synchronisation promiscuity, oscillation strength, and orientation selectivity. Our results predict that SHs receive relatively strong rhythmic inhibition, and, consequently, exhibit strong oscillations across a broad range of stimulus orientations. Such rhythmic inhibition provides a temporal framework that promotes synchrony by establishing and coordinating coherent, narrow windows of enhanced firing in its postsynaptic targets.

Excitatory neurons are known to receive rhythmic inhibitory inputs during gamma oscillations (Ferster, 1986; Hasenstaub *et al.*, 2005; Buzsaki & Wang, 2012). Neurons in area 17 exhibit diversity in orientation selectivity, with stronger inhibition being consistent with sharper orientation tuning (Sillito, 1975; Ringach *et al.*, 1997; Sompolinsky & Shapley, 1997; Crook *et al.*, 1998; Shapley *et al.*, 2007; Liu *et al.*, 2011; Li *et al.*, 2012) (however, see Finn *et al.*, 2007; Li *et al.*, 2008; Liu *et al.*, 2011). Studies have also revealed heterogeneity in the tuning of inhibition, with inhibition more broadly tuned than excitation in some cases (Sato *et al.*, 1996; Roerig & Chen, 2002; Monier *et al.*, 2003; Nowak *et al.*, 2008). In a study providing additional support for our conclusions, Li *et al.* (2008) investigated the effects of both GABA and bicuculline on neurons in cat area 17 that were weakly, moderately, and strongly orientation selective. The $GABA_A$ antagonist bicuculline diminished

orientation selectivity to the largest extent in strongly selective neurons and had minimal effects on the weakly orientation-selective neurons. However, applying GABA had the strongest effect of enhancing orientation selectivity in weakly selective neurons and minimal effects on strongly selective neurons. These results are consistent with our notion that stronger inhibition leads to higher orientation selectivity. Another recent study demonstrated more directly the relation between inhibition and tuning properties in the V1. Optogenetic activation of GABAergic interneurons in the mouse V1 enhances orientation selectivity as well as perceptual discrimination (Lee *et al.*, 2012; see also Wilson *et al.*, 2012). Additionally, we observed a loss of coherent oscillatory patterning and a drop in synchrony in our recordings of pairs of units separated by distances > 1 mm. This observation is consistent with the findings of Albus *et al.* (1991), who reported in cat area 17 that 70% of the axons of GABAergic neurons in layers II/III project over a region < 1 mm. This indicates that units separated by > 1 mm are less likely to receive coherent inhibition than more proximal units.

Mechanisms other than rhythmic inhibition could produce oscillations and synchronisation in neuronal firing. However, it is unclear whether they can explain how these properties correlate across neurons. For example, broadly tuned sensory-induced excitatory inputs to a subset of area 17 neurons could promote synchronisation with cells of different orientation preferences. This would imply that SHs are more broadly tuned; however, we find that SHs are more sharply tuned (see also Yu *et al.*, 2008). The sharp tuning of SHs also suggests that they might lie in regions of homogeneous orientation preference (Nauhaus *et al.*, 2008), making it less likely that they synchronise promiscuously as a consequence of direct excitatory input from cells with other preferences (Schummers *et al.*, 2002; Mariño *et al.*, 2005). If SHs did receive strong levels of rhythmic excitation, then the weaker rhythmic excitation to nSHs would need to be compensated by stronger non-rhythmic excitation to maintain equal firing rates at preferred orientations. Although it is theoretically possible to adjust such inputs to achieve sharper tuning and stronger oscillations, to our knowledge such a negatively correlated balance of excitatory inputs has not been observed experimentally. Furthermore, to produce strong synchronisation, rhythmic excitatory signals would need to be in phase across different neurons and sufficiently narrowly distributed in their arrival times. In contrast, excitatory synapses are distributed across dendritic trees and dendrites filter excitatory input. Hence, the resultant blurring and delaying of rhythmic excitatory signals (Magee, 2000; London *et al.*, 2010; Branco & Häusser, 2011) limits the plausibility of these excitation-based mechanisms to produce robust in-phase oscillations in the network.

A compelling feature of our model is that it is general in two important ways. First, we did not make any *a-priori* assumptions about the particular source and mechanism for the prescribed synaptic currents. Second, although our recordings were conducted in the visual cortex, our modeling results apply more generally to brain regions with analogous anatomy. The simplicity of our model, based on prescribed inputs to a small set of unconnected neurons, allows efficient exploration of the effects of rhythmic inhibition (and excitation). In a future study, it would be interesting to explore similar ideas in a larger, interconnected model network of excitatory and inhibitory neurons, featuring heterogeneous coupling strengths that generate gamma oscillations and orientation tuning autonomously. In such a network, when tuned to produce gamma oscillations, we predict that neurons receiving relatively strong inhibition over a wide range of orientations will (i) synchronise promiscuously, (ii) exhibit narrow orientation tuning curves, and (iii) feature a high degree of oscillatory patterning in their firing output, thus emerging as SHs. Inclusion of various intrinsic ionic currents could also add further realism to a future model. For example, our preliminary explorations of conductance-based models with calcium currents that induce bursting (data not shown) produced analogous results to those herein but additionally produced ACHs that resemble those from SUA in our experimental recordings that did not exhibit a pronounced gap in coincidences near zero lag. However, a shortcoming of such studies is that generating smooth ACH/CCHs from such simulations is numerically intensive, which severely limits the parameters and types of conductance-based models that can be explored.

At present we are unsure what the functional role of SHs may be. Nevertheless, there are several possibilities. Attention and expectation can modulate the strength of gamma oscillations (Fries *et al.*, 2007; Chalk *et al.*, 2010; Lima *et al.*, 2011). Given that SHs exhibit particularly strong gamma oscillations, and given that similar gamma oscillations appear to emerge from similar mechanisms in awake and anaesthetised states (Xing *et al.*, 2012), variations in inhibitory signaling may therefore play a role in attentional mechanisms. Similarly, SHs may also play a role in the strongly coherent gamma oscillations that are proposed to contribute to communication between neuronal populations (Schoffelen *et al.*, 2005; Fries *et al.*, 2007; Tiesinga & Sejnowski, 2010). Finally, gamma oscillations and synchrony shaped by SHs may drive coding based on relative spike timing (Nikolić, 2007; Havenith *et al.*, 2011) .

In conclusion, heterogeneity in the strength of coherent rhythmic inhibition offers a parsimonious way to explain how oscillation strength, synchronisation promiscuity, and orientation selectivity could covary in a network of excitatory neurons during gamma oscillations as we have shown occurs in cat area 17. In particular, neurons receiving the strongest inhibitory inputs are capable of synchronising promiscuously across orientations and could serve as SHs in the network. Future experiments should characterise the properties of inhibitory inputs to excitatory neurons during gamma oscillations. These efforts could be quite informative for elucidating the importance of this putative heterogeneity for stimulus encoding and processing.

Supporting Information

Additional supporting information can be found in the online version of this article:

Figure S1. Analogous results to those in Figure 3 of the main paper, showing the significant correlation between synchrony strength, orientation bias, and oscillation strength, with oscillation strength and synchrony strength computed only at the preferred orientation (optimally stimulated).

Figure S2. Analogue of Figure S1, showing the significant correlation between synchrony strength and orientation bias/oscillation strength, with synchrony strength calculated using scaled correlation at the preferred orientation.

Figure S3. Orientation bias (A,D), oscillation strength (B,E), and synchrony strength (C,F) reveal no trend with respect to the peak firing rate response.

Figure S4. Analogous results to those in Figure 3 of the main paper and Figure S1 for the case of the coincidence measure (instead of the synchrony strength) computed only at the preferred orientation (optimally stimulated).

Figure S5. Variability in the gamma cycle length attenuates the satellite peaks in the CCH/ACHs.

Acknowledgements

This work was supported by the U.S. National Science Foundation (grant number EMSW21-RTG 0739261, DMS-1021701), Deutsche Forschungsgemeinschaft (grant number NI 708/2-1), Hertie Foundation, Alexander von Humboldt Stiftung, LOEWE Neuronale Koordination Forschungsschwerpunkt Frankfurt (NeFF), Max-Planck Geselschaft, and Frankfurt Institute for Advanced Studies.

Abbreviations

ACH, autocorrelation histogram; CCH, crosscorrelation histogram; MUA, multi-unit activity; nSH, not a synchronisation hub; SH, synchronisation hub; SUA, single-unit activity.

References

Albus, K., Wahle, P., Lübke, J. & Matute, C. (1991) The contribution of GABA-ergic neurons to horizontal intrinsic connections in upper layers of the cat's striate cortex. *Exp. Brain Res.*, **85**, 235–239.

Amari, S.-I. (2009) Measure of correlation orthogonal to change in firing rate. *Neural Comput.*, **21**, 960–972.

Anderson, J.S., Carandini, M. & Ferster, D. (2000) Orientation tuning of input conductance, excitation, and inhibition in cat primary visual cortex. *J. Neurophysiol.*, **84**, 909–926.

Atallah, B.V. & Scanziani, M. (2009) Instantaneous modulation of gamma oscillation frequency by balancing excitation with inhibition. *Neuron*, **62**, 566–577.

Bartos, M., Vida, I. & Jonas, P. (2007) Synaptic mechanisms of synchronized gamma oscillations in inhibitory interneuron networks. *Nat. Rev. Neurosci.*, **8**, 45–56.

Blasdel, G.G. (1992) Orientation selectivity, preference, and continuity in monkey striate cortex. *J. Neurosci.*, **12**, 3139–3161.

Bonds, A.B. (1989) Role of inhibition in the specification of orientation selectivity of cells in the cat striate cortex. *Visual Neurosci.*, **2**, 41–55.

Bonifazi, P., Goldin, M., Picardo, M.A., Jorquera, I., Cattani, A., Bianconi, G., Represa, A., Ben-Ari, Y. & Cossart, R. (2009) GABAergic hub neurons orchestrate synchrony in developing hippocampal networks. *Science*, **326**, 1419–1424.

Börgers, C. & Kopell, N. (2003) Synchronization in networks of excitatory and inhibitory neurons with sparse, random connectivity. *Neural Comput.*, **15**, 509–538.

Bosking, W.H., Zhang, Y., Schofield, B. & Fitzpatrick, D. (1997) Orientation selectivity and the arrangement of horizontal connections in tree shrew striate cortex. *J. Neurosci.*, **17**, 2112–2127.

Branco, T. & Häusser, M. (2011) Synaptic integration gradients in single cortical pyramidal cell dendrites. *Neuron*, **69**, 885–892.

Buhl, E., Tamás, G. & Fisahn, A. (1998) Cholinergic activation and tonic excitation induce persistent gamma oscillations in mouse somatosensory cortex *in vitro*. *J. Physiol.*, **513**, 117–126.

Buzsaki, G. & Wang, X.-J. (2012) Mechanisms of gamma oscillations. *Annu. Rev. Neurosci.*, **35**, 203–225.

Cardin, J.A., Carlén, M., Meletis, K., Knoblich, U., Zhang, F., Deisseroth, K., Tsai, L.-H. & Moore, C.I. (2009) Driving fast-spiking cells induces gamma rhythm and controls sensory responses. *Nature*, **459**, 663–667.

Chalk, M., Herrero, J., Gieselmann, M. & Delicato, L. (2010) Attention reduces stimulus-driven gamma frequency oscillations and spike field coherence in V1. *Neuron*, **66**, 114–125.

Crook, J.M., Kisvárday, Z.F. & Eysel, U.T. (1998) Evidence for a contribution of lateral inhibition to orientation tuning and direction selectivity in cat visual cortex, reversible inactivation of functionally characterized sites combined with neuroanatomical tracing techniques. *Eur. J. Neurosci.*, **10**, 2056–2075.

Csicsvari, J., Jamieson, B., Wise, K. & Buzsáki, G. (2003) Mechanisms of gamma oscillations in the hippocampus of the behaving rat. *Neuron*, **37**, 311–322.

Cunningham, M.O., Davies, C., Buhl, E.H., Kopell, N. & Whittington, M.A. (2003) Gamma oscillations induced by kainate receptor activation in the entorhinal cortex *in vitro*. *J. Neurosci.*, **23**, 9761–9769.

Dayan, P. & Abbott, L.F. (2005) *Theoretical Neuroscience*. MIT Press, Cambridge.

Dickson, C., Biella, G. & de Curtis, M. (2000) Evidence for spatial modules mediated by temporal synchronization of carbachol-induced gamma rhythm in medial entorhinal cortex. *J. Neurosci.*, **20**, 7846–7854.

Doiron, B., Chacron, M.J., Maler, L., Longtin, A. & Bastian, J. (2003) Inhibitory feedback required for network oscillatory responses to communication but not prey stimuli. *Nature*, **421**, 539–543.

Ferster, D. (1986) Orientation selectivity of synaptic potentials in neurons of cat primary visual cortex. *J. Neurosci.*, **6**, 1284–1301.

Finn, I., Priebe, N.J. & Ferster, D. (2007) The emergence of contrast-invariant orientation tuning in simple cells of cat visual cortex. *Neuron*, **54**, 137–152.

Fisahn, A., Pike, F.G., Buhl, E.H. & Paulsen, O. (1998) Cholinergic induction of network oscillations at 40 Hz in the hippocampus *in vitro*. *Nature*, **394**, 186–189.

Freund, T.F. (2003) Interneuron diversity series, rhythm and mood in perisomatic inhibition. *Trends Neurosci.*, **26**, 489–495.

Fries, P., Nikolić, D. & Singer, W. (2007) The gamma cycle. *Trends Neurosci.*, **30**, 309–316.

Gilbert, C.D. & Wiesel, T.N. (1983) Clustered intrinsic connections in cat visual cortex. *J. Neurosci.*, **3**, 1116–1133.

Gloveli, T., Dugladze, T., Saha, S., Monyer, H., Heinemann, U., Traub, R.D., Whittington, M.A. & Buhl, E.H. (2005) Differential involvement of oriens/pyramidale interneurones in hippocampal network oscillations *in vitro*. *J. Physiol.*, **562**, 131–147.

Gray, C.M. & Singer, W. (1989) Stimulus-specific neuronal oscillations in orientation columns of cat visual cortex. *Proc. Natl. Acad. Sci. USA*, **86**, 1698–1702.

Gray, C.M., König, P., Engel, A. & Singer, W. (1989) Oscillatory responses in cat visual cortex exhibit inter-columnar synchronization which reflects global stimulus properties. *Nature*, **338**, 334–337.

Hasenstaub, A., Shu, Y., Haider, B., Kraushaar, U., Duque, A. & McCormick, D. (2005) Inhibitory postsynaptic potentials carry synchronized frequency information in active cortical networks. *Neuron*, **47**, 423–435.

Havenith, M.N., Yu, S., Biederlack, J., Chen, N.H., Singer, W. & Nikolić, D. (2011) Synchrony makes neurons fire in sequence, and stimulus properties determine who is ahead. *J. Neurosci.*, **31**, 8570–8584.

Isaacson, J.S. & Scanziani, M. (2011) How inhibition shapes cortical activity. *Neuron*, **72**, 231–243.

Kisvárday, Z.F. & Eysel, U.T. (1993) Functional and structural topography of horizontal inhibitory connections in cat visual cortex. *Eur. J. Neurosci.*, **5**, 1558–1572.

Lee, S.-H., Kwan, A.C., Zhang, S., Phoumthipphavong, V., Flannery, J.G., Masmanidis, S.C., Taniguchi, H., Huang, Z.J., Zhang, F., Boyden, E.S., Deisseroth, K. & Dan, Y. (2012) Activation of specific interneurons improves V1 feature selectivity and visual perception. *Nature*, **488**, 379–383.

Leventhal, A.G., Thompson, K.G., Liu, D., Zhou, Y. & Ault, S.J. (1995) Concomitant sensitivity to orientation, direction, and color of cells in layers 2, 3, and 4 of monkey striate cortex. *J. Neurosci.*, **15**, 1808–1818.

Li, G., Yang, Y., Liang, Z., Xia, J., Yang, Y. & Zhou, Y. (2008) GABA-mediated inhibition correlates with orientation selectivity in primary visual cortex of cat. *Neuroscience*, **155**, 914–922.

Li, Y.-T., Ma, W.-P., Pan, C.-J., Zhang, L.I. & Tao, H.W. (2012) Broadening of cortical inhibition mediates developmental sharpening of orientation selectivity. *J. Neurosci.*, **32**, 3981–3991.

Lima, B., Singer, W. & Neuenschwander, S. (2011) Gamma responses correlate with temporal expectation in monkey primary visual cortex. *J. Neurosci.*, **31**, 15919–15931.

Liu, B.-H., Li, Y.-T., Ma, W.-P., Pan, C.-J., Zhang, L.I. & Tao, H.W. (2011) Broad inhibition sharpens orientation selectivity by expanding input dynamic range in mouse simple cells. *Neuron*, **71**, 542–554.

London, M., Roth, A., Beeren, L., Häusser, M. & Latham, P.E. (2010) Sensitivity to perturbations *in vivo* implies high noise and suggests rate coding in cortex. *Nature*, **466**, 123–127.

Magee, J.C. (2000) Dendritic integration of excitatory synaptic input. *Nat. Rev. Neurosci.*, **1**, 181–190.

Mariño, J., Schummers, J., Lyon, D., Schwabe, L., Beck, O., Wiesing, P., Obermayer, K. & Sur, M. (2005) Invariant computations in local cortical networks with balanced excitation and inhibition. *Nat. Neurosci.*, **8**, 194–201.

Martin, K., Somogyi, P. & Whitteridge, D. (1983) Physiological and morphological properties of identified basket cells in the cat's visual cortex. *Exp. Brain Res.*, **50**, 193–200.

Middleton, S., Jalics, J., Kispersky, T., LeBeau, F., Roopun, A., Kopell, N., Whittington, M.A. & Cunningham, M.O. (2008) NMDA receptor-dependent switching between different gamma rhythm-generating microcircuits in entorhinal cortex. *Proc. Natl. Acad. Sci. USA*, **105**, 18572–18577.

Monier, C., Chavane, F., Baudot, P., Graham, L. & Frégnac, Y. (2003) Orientation and direction selectivity of synaptic inputs in visual cortical neurons, a diversity of combinations produces spike tuning. *Neuron*, **37**, 663–680.

Muresan, R.C., Jurjut, O.F., Moca, V.V., Singer, W. & Nikolić, D. (2008) The oscillation score, an efficient method for estimating oscillation strength in neuronal activity. *J. Neurophysiol.*, **99**, 1333–1353.
Nauhaus, I., Benucci, A., Carandini, M. & Ringach, D.L. (2008) Neuronal selectivity and local map structure in visual cortex. *Neuron*, **57**, 673–679.
Nikolić, D. (2007) Non-parametric detection of temporal order across pairwise measurements of time delays. *J. Comput. Neurosci.*, **22**, 5–19.
Nikolić, D. (2009) Model this! seven empirical phenomena missing in the models of cortical oscillatory dynamics. *IEEE IJCNN*, **2009**, 2272–2279.
Nikolić, D., Mureşan, R.C., Feng, W. & Singer, W. (2012) Scaled correlation analysis: a better way to compute a cross-correlogram. *Eur. J. Neurosci.*, **35**, 742–762.
Nowak, L.G., Sanchez-Vives, M.V. & McCormick, D.A. (2008) Lack of orientation and direction selectivity in a subgroup of fast-spiking inhibitory interneurons: cellular and synaptic mechanisms and comparison with other electrophysiological cell types. *Cereb. Cortex*, **18**, 1058–1078.
Ringach, D.L., Hawken, M.J. & Shapley, R.M. (1997) Dynamics of orientation tuning in macaque primary visual cortex. *Nature*, **387**, 281–284.
Ringach, D.L., Shapley, R.M. & Hawken, M.J. (2002) Orientation selectivity in macaque V1: diversity and laminar dependence. *J. Neurosci.*, **22**, 5639–5651.
Roerig, B. & Chen, B. (2002) Relationships of local inhibitory and excitatory circuits to orientation preference maps in ferret visual cortex. *Cereb. Cortex*, **12**, 187–198.
Roudi, Y., Nirenberg, S. & Latham, P.E. (2009) Pairwise maximum entropy models for studying large biological systems, when they can work and when they can't. *PLoS Comput. Biol.*, **5**, e1000380.
Samonds, J. & Bonds, A. (2005) Gamma oscillation maintains stimulus structure-dependent synchronization in cat visual cortex. *J. Neurophysiol.*, **93**, 223–236.
Sato, H., Katsuyama, N., Tamura, H., Hata, Y. & Tsumoto, T. (1996) Mechanisms underlying orientation selectivity of neurons in the primary visual cortex of the macaque. *J. Physiol.*, **494**, 757–771.
Schoffelen, J.-M., Oostenveld, R. & Fries, P. (2005) Neuronal coherence as a mechanism of effective corticospinal interaction. *Science*, **308**, 111–113.
Schummers, J., Mariño, J. & Sur, M. (2002) Synaptic integration by V1 neurons depends on location within the orientation map. *Neuron*, **36**, 969–978.
Shapley, R., Hawken, M. & Xing, D. (2007) The dynamics of visual responses in the primary visual cortex. *Prog. Brain Res.*, **165**, 21–32.
Sillito, A.M. (1975) The contribution of inhibitory mechanisms to the receptive field properties of neurones in the striate cortex of the cat. *J. Physiol.*, **250**, 305–329.
Sohal, V., Zhang, F., Yizhar, O. & Deisseroth, K. (2009) Parvalbumin neurons and gamma rhythms enhance cortical circuit performance. *Nature*, **459**, 698–702.
Somogyi, P., Kisvárday, Z.F., Martin, K.A. & Whitteridge, D. (1983) Synaptic connections of morphologically identified and physiologically characterized large basket cells in the striate cortex of cat. *Neuroscience*, **10**, 261–294.
Sompolinsky, H. & Shapley, R.M. (1997) New perspectives on the mechanisms for orientation selectivity. *Curr. Opin. Neurobiol.*, **7**, 514–522.
Tamás, G., Buhl, E.H., Lörincz, A. & Somogyi, P. (2000) Proximally targeted GABAergic synapses and gap junctions synchronize cortical interneurons. *Nat. Neurosci.*, **3**, 366–371.
Tiesinga, P.H.E. & Sejnowski, T.J. (2010) Mechanisms for phase shifting in cortical networks and their role in communication through coherence. *Front. Hum. Neurosci.*, **4**, 196.
Tiesinga, P.H.E., Fellous, J.M., José, J.V. & Sejnowski, T.J. (2001) Computational model of carbachol-induced delta, theta, and gamma oscillations in the hippocampus. *Hippocampus*, **11**, 251–274.
Traub, R.D., Whittington, M.A., Colling, S.B., Buzsaki, G. & Jefferys, J.G. (1996) Analysis of gamma rhythms in the rat hippocampus *in vitro* and *in vivo*. *J. Physiol.*, **493**, 471–484.
Traub, R.D., Bibbig, A., Fisahn, A., LeBeau, F.E., Whittington, M.A. & Buhl, E.H. (2000) A model of gamma-frequency network oscillations induced in the rat CA3 region by carbachol *in vitro*. *Eur. J. Neurosci.*, **12**, 4093–4106.
Traub, R.D., Bibbig, A., LeBeau, F.E., Cunningham, M.O. & Whittington, M.A. (2005) Persistent gamma oscillations in superficial layers of rat auditory neocortex, experiment and model. *J. Physiol.*, **562**, 3–8.
van Vreeswijk, C., Abbott, L. & Ermentrout, G.B. (1994) When inhibition not excitation synchronizes neural firing. *J. Comput. Neurosci.*, **1**, 313–321.
Wang, X-J. & Buzsaki, G. (1996) Gamma oscillation by synaptic inhibition in a hippocampal interneuronal network model. *J. Neurosci.*, **16**, 6402–6413.
White, J., Chow, C., Ritt, J., Soto-Trevino, C. & Kopell, N. (1998) Synchronization and oscillatory dynamics in heterogeneous mutually inhibited neurons. *J. Comput. Neurosci.*, **5**, 5–16.
Whittington, M.A., Traub, R.D. & Jefferys, J.G. (1995) Synchronized oscillations in interneuron networks driven by metabotropic glutamate receptor activation. *Nature*, **373**, 612–615.
Whittington, M.A., Traub, R.D., Kopell, N., Ermentrout, B. & Buhl, E.H. (2000) Inhibition-based rhythms, experimental and mathematical observations on network dynamics. *Int. J. Psychophysiol.*, **38**, 315–336.
Whittington, M.A., Cunningham, M.O., Lebeau, F.E., Racca, C. & Traub, R.D. (2010) Multiple origins of the cortical gamma rhythm. *Dev. Neurobiol.*, **71**, 92–106.
Wilson, N.R., Runyan, C.A., Wang, F.L. & Sur, M. (2012) Division and subtraction by distinct cortical inhibitory networks *in vivo*. *Nature*, **488**, 343–348.
Xing, D., Shen, Y., Burns, S., Yeh, C.-I., Shapley, R. & Li, W. (2012) Stochastic generation of gamma-band activity in primary visual cortex of awake and anesthetized monkeys. *J. Neurosci.*, **32**, 13873–13880.
Yu, S., Huang, D., Singer, W. & Nikolić, D. (2008) A small world of neuronal synchrony. *Cereb. Cortex*, **18**, 2891–2901.

Appendix

Normalised spike count histogram, crosscorrelation, and coincident spikes

As described in the Materials and methods, the spike count histograms in Fig. 8A and C were constructed for neuron j by (i) rescaling each cycle length to match the trial-averaged cycle length $T = \omega^{-1}(1000$ ms/s) for all trials where ω is the average gamma frequency for all trials, (ii) converting the spike time within a cycle to the relative phase (between 0 at the beginning of the cycle and T at the end of the normalised cycle), (iii) constructing the cycle-averaged spike count histogram $S_j(n)$ from the distribution of spikes according to a partitioning of the normalised cycle $[0,T]$ into N_{bin} phase bins and dividing the trial-averaged spiked count in each phase bin by the average number of cycles N_{cycle} per trial, and finally (iv) constructing the normalised cycle-averaged spike count histogram $s_j(n)$ by scaling $S_j(n)$ by the baseline cycle-averaged spike count per bin $B_j = N_j/N_{\text{bin}}N_{\text{cycle}}$ for neuron j, i.e.

$$s_j(n) = \frac{S_j(n)}{B_j}$$

where N_j is the trial-averaged spike count for neuron j. The value $S_j(n)$ can be interpreted as the trial-averaged fraction of cycles in which a spike occurred in phase bin n. As the histogram $S_j(n)$ for any neuron j is defined on the normalised cycle $[0,T]$, it can be extended periodically, and the crosscorrelation $S_i \star S_j$ between the histograms for neuron i and neuron j can be calculated as

$$(S_i \bigstar S_j)(n) = \sum_{m=1}^{N_{\text{bin}}} S_i(m) S_j(n+m)$$

where $-N_{\text{bin}} \le n \le 0$ corresponds to $[-T,0]$. The quantities $S_i(n)$ and $S_j(n)$, respectively, represent the trial-averaged fractions of cycles in which neuron i and neuron j individually fire a spike in phase bin n, which effectively represent the cycle-averaged probabilities that neurons i and j individually fire a spike in phase bin n (as the probability itself can fluctuate cycle by cycle). As the spiking in neurons i and j is approximately independent (over the time course of a bin that is sufficiently short relative to the length of the gamma cycle, the features of the synaptic inputs that induce correlations through changes in the neuronal spiking vary sufficiently slowly that

they can be taken to be approximately constant), then $(S_i \star S_j)$ (0) represents the cycle-averaged probability that neurons i and j fire a coincident spike in the same phase bin and, more generally, $(S_i \star S_j)$ (n) represents the cycle-averaged probability that the two neurons fire a coincident spike in phase bins separated by a lag of $(n/N_{\text{bin}})T$. (Note that as the neurons fire sparsely and skip cycles, the cycle-averaged probability of firing on any cycle is less than 1.)

For any two spike histograms that are uniform at the baseline level, i.e. $S_i(n) = S_i^{\text{base}}(n) \equiv B_i$ and $S_j(n) = S_j^{\text{base}}(n) \equiv B_j$ for all n, the cycle-averaged probability that neurons i and j fire a spike in phase bins separated by a lag of $(n/N_{\text{bin}})T$ is given by the uniform histogram

$$(S_i^{\text{base}} \bigstar S_j^{\text{base}})(n) = \sum_{m=1}^{N_{\text{bin}}} B_i B_j = N_{\text{bin}} B_i B_j$$

(Note that, in the uniform baseline case, this indicates that the average probability of coincident spikes occurring between neurons i and j increases if the average firing rates of the neurons increase.) From this we see that the quantity $(1/N_{\text{bin}})$ $(s_i \star s_j)$ (n), which can be expressed as

$$\frac{1}{N_{\text{bin}}}(s_i \bigstar s_j)(n) = \frac{1}{N_{\text{bin}}} \sum_{m=1}^{N_{\text{bin}}} \frac{S_i(m)}{B_i} \frac{S_j(n+m)}{B_j} = \frac{\sum_{m=1}^{N_{\text{bin}}} S_i(m) S_j(n+m)}{N_{\text{bin}} B_i B_j}$$

represents the ratio of the cycle-averaged probability that neurons i and j fire spikes separated by a lag of $(n/N_{\text{bin}})T$ during each cycle relative to the cycle-averaged probability in the uniform baseline case. Importantly, as the synchrony strength between two neurons is not only affected by the shaping of the windows of enhanced firing but also the average firing rates of the neurons, the scaling by baseline identifies the degree to which the shaping of the windows of enhanced firing increases the probability of coincident spikes relative to baseline, allowing for a more direct comparison of this effect between pairings of neurons exhibiting different firing rates. This not only applies to $(1/N_{\text{bin}})$ $(s_i \star s_j)$ but also to the normalised CCHs in Fig. 8B, which are scaled by the baseline number of coincidences for each pairing.

The matching of the plots in Fig. 8C, of $(1/N_{\text{bin}})$ $(s_i \star s_j)$ [which measures the probability of coincident spikes at lags $(n/N_{\text{bin}})T$] and the CCH [which measures the actual number of coincident spikes at lags $(n/N_{\text{bin}})T$], consistent with the Law of Large Numbers, shows that the increase in probability of coincident spiking relative to baseline due to the shaping of the windows of enhanced firing results in a commensurate increase in the number of coincident spikes relative to baseline found in realisations of the model.

Finally, we mention that, in the coincidence measure, we considered coincident spikes to be those with spike time differences of less than 3 ms, which, in the context of $(1/N_{\text{bin}})$ $(s_i \star s_j)$, would span $(2m + 1)$ phase lag bins about $n = 0$, where $1 < m \ll N_{\text{bin}}$ depends on the value of the average cycle length T. Consequently, the coincidence measure would correspond to the increase above 1 in the ratio of the cycle-averaged probability of coincident spikes to the cycle-averaged probability in the baseline case, i.e.

$$\left[\sum_{n=-m}^{m} \frac{1}{N_{\text{bin}}} (s_i \bigstar s_j)(n) \right] - 1$$